HyTC-TaNet: A Hybrid Deep Learning Model Capturing Multi-day Temporal Dependencies for Daily Mean Air Temperature Estimation with Spatial Applicability Analysis

Li Liu [a, b, c], Cian Yuan [a, b], Jingfeng Huang [d], Yi Yu [e, f], Pan Shao [b], Junbo Yu [a, b, c], Lu Wang [a, b, c], Ran Huang [g, *], Dong Ren [a, b, c, *], Thomas F. A. Bishop [e, h]

Affiliations:

[a] Hubei Key Laboratory of Intelligent Vision Based Monitoring for Hydroelectric Engineering, China Three Gorges University, Yichang 443002, China

[b] College of Computer and Information Technology, China Three Gorges University, Yichang 443002, China

[c] Hubei Engineering Technology Research Center for Farmland Environment Monitoring, China Three Gorges University, Yichang, 443002, China

[d] Institute of Applied Remote Sensing and Information Technology, Zhejiang University, Hangzhou 310058, China

[e] Sydney Institute of Agriculture, School of Life and Environmental Sciences, The University of Sydney, Eveleigh, NSW 2015, Australia

[f] CSIRO Agriculture and Food, Canberra, ACT 2601, Australia

[g] School of Automation, Hangzhou Dianzi University, Xiasha Higher Education Zone, Hangzhou 310018, China

[h] Sydney Informatics Hub, The University of Sydney, Newtown, NSW 2042, Australia

Corresponding Author:

Ran Huang

Email: ran_huang@hdu.edu.cn

Dong Ren

Email: dren@ctgu.edu.cn

Statement: This manuscript is a preprint submitted to **EarthArXiv** and has not been peer-reviewed.

Abstract

Air temperature is a fundamental indicator for climate monitoring, agricultural planning, and ecosystem management. Land Surface Temperature (LST) retrieved from thermal remote sensing is widely used as a critical proxy due to its strong physical coupling with air temperature. However, existing air temperature estimation studies predominantly rely on single-date LST and diurnal variations (e.g., the Diurnal Temperature Cycle, DTC), overlooking systematic investigations into the potential of multi-day time series and lacking explicit consideration of spatial representativeness. These limitations hinder the exploration of temporal dependencies and limit the assessment of spatial representativeness. To address these challenges, here we present a hybrid Transformer-CNN daily mean air temperature (Ta) estimation network (HyTC-TaNet) which integrates Transformer-based temporal attention with convolutional feature extraction. Specifically, this architecture facilitates the expansion of temporal modeling from the DTC to multi-day temporal patterns, while the Area of Applicability (AOA) metric is introduced to quantify spatial prediction confidence. Comparative experiments involving eight models, including HyTC-TaNet and seven benchmark algorithms, reveal that a 6-7 days temporal input window yields the best performance across all models. HyTC-TaNet achieves the highest accuracy, with RMSE = 1.429 °C, MAE = 1.101 °C, and R^2 = 0.976, reducing errors by 0.273 °C (RMSE) and 0.219 °C (MAE) compared with concurrent day input. Spatial-temporal analysis further confirms that the optimal temporal sequence enriches historical and trend information, significantly enhancing estimation stability and spatial detail. Furthermore, the AOA of the model was assessed, confirming robust applicability in station-dense plains while effectively flagging extrapolation risks over large water bodies and high-altitude ridges due to limited representativeness in the training data. These findings demonstrate the strong potential of coupling HyTC-TaNet with optimally selected multi-day time series and spatial applicability assessment for precise, scalable air temperature estimation.

Keywords: Air temperature estimation, Temporal dependency, Hybrid Transformer network, Multi-day Land surface temperature, optimal temporal sequence, Area of applicability (AOA)

1. Introduction

Air temperature, as a core parameter representing land surface energy balance and land-atmosphere interactions, is not only a fundamental variable in meteorological research but also an essential reference for agricultural production and forest ecosystem management (Abhishek et al., 2023; Benali et al., 2012; Overland et al., 2019; Shanmugapriya et al., 2019; Ueyama, 2024). Variations in air temperature directly influence the occurrence and severity of agro-meteorological disasters, including heat stress, cold spells, and compound heat-drought events (Dou et al., 2020; Huang et al., 2025a; Li et al., 2021; Ma et al., 2022; Wei et al., 2024). Consequently, accurate monitoring of air temperature is essential for evaluating climate suitability, developing disaster mitigation strategies, and supporting sustainable ecosystem management (Ji et al., 2014; Robeson, 2002; Shin et al., 2020).

Conventional air temperature observations are primarily derived from standard meteorological stations installed about 2 m above the ground. However, in regions characterized by complex topography or sparse infrastructure, the spatial coverage of these stations is highly uneven. Traditional interpolation techniques can partially bridge the observational gaps but often suffer from low accuracy and data discontinuity, particularly when applied to high-resolution or long-term temperature reconstruction over heterogeneous terrains (Chung et al., 2006; Wu and Li, 2013).

Recent advances in satellite remote sensing have significantly enhanced large-scale air temperature estimation, providing valuable spatially continuous datasets with high temporal resolution (Gao et al., 2021; Hooker et al., 2018; Zhang et al., 2016). These approaches leverage the strong physical coupling between land surface temperature (LST), retrieved from thermal infrared remote sensing, and near-surface air temperature, as both are linked through surface-atmosphere energy fluxes (Sohrabinia et al., 2015). Compared with ground-based data, satellite observations offer superior spatial completeness and regional representativeness (Good, 2016; Lin et al., 2012; Liu et al., 2022). Notably, previous research has successfully developed LST products exhibiting high temporal and spatial continuity, effectively resolving data discontinuities induced by cloud cover, sensor degradation, and related factors (Xu and Cheng, 2021; Yu et al., 2024; Zhang et al., 2022). This has provided reliable support for constructing complete LST time series, making air temperature estimation based on LST time series data feasible.

Current air temperature estimation methods using remote sensing data are mainly divided into three categories: the Temperature-Vegetation Index (TVX) method (Nieto et al., 2011; Prihodko and Goward, 1997; Zhang et al., 2014; Zhu et al., 2013), energy balance methods and statistical methods (Hou et al., 2013; Pape and Löffler, 2004; Sun et al., 2005; Zhang et al., 2015). Among these, statistical methods, especially those incorporating multiple predictors, are most widely used due to their flexibility and relatively low computational demand. Such methods, including multiple linear regression and machine learning algorithms, can model nonlinear relationships between LST, vegetation indices, and meteorological variables to improve estimation accuracy(Carrión et al., 2021). In addition, hybrid estimation strategies fusing physical mechanisms (like TVX) and data-driven machine learning are becoming increasingly prominent. By integrating the strong nonlinear mapping capability of machine learning with the explicit physical meaning of TVX, these methods aim to refine air temperature estimation models. For example, (Xu et al., 2023)) integrated remote sensing, meteorological observations, and assimilation data using a Random Forest framework to estimate Ta across winter wheat fields in Henan Province, achieving superior accuracy when combining the TVX index with machine learning.

However, most existing approaches employ a single-timeframe data fusion strategy, overlooking the inherent temporal dynamics of air temperature as a continuously evolving climatic variable (Chen et al., 2021; Huang et al., 2025b; Wang et al., 2024). Physically, air temperature is a continuous trajectory governed by the cumulative heat storage and the lifecycle of synoptic weather systems (Hartmann, 2016). Crucially, previous studies have confirmed that LST and air temperature exhibit remarkably synchronized temporal patterns (Good et al., 2017), providing a robust physical foundation for time-series-based estimation. Yet, due to the thermal inertia of the underlying surface, there remains a thermodynamic phase shift between energy input and the temperature response. Reliance on instantaneous or single-date LST fails to capture this cumulative heating effect, leading to insufficient constraints on the energy balance equation. Furthermore, from the perspective of atmospheric memory, historical data within the decorrelation time scale contains valid predictive signals essential for stabilizing estimations against short-term noise. Consequently, exploring the optimal sequence length for estimation is crucial; an overly short temporal window may miss the synoptic context, while an excessively long window risks introducing information redundancy.

Beyond data dimensionality, structural limitations also constrain model performance. Traditional regression and classic machine learning methods are efficient, yet they struggle to capture complex spatiotemporal nonlinearities and often face issues such as overfitting or local convergence (Bay and Yearick, 2024). Deep learning techniques, with their hierarchical feature extraction and strong generalization capacity, provide new opportunities for modeling the spatiotemporal variability of air temperature. For example, Shen et al. (2020) proposed a Deep Belief Network (DBN) integrating multi-source data for daily maximum temperature estimation, while Yang et al. (2024) introduced TaNet, an encoder-decoder neural network leveraging FY-4A satellite imagery for high-resolution air temperature retrieval (Yang et al., 2024). Despite these advances, most deep learning frameworks remain static in their input design, failing to fully exploit the temporal dependencies among multi-source time series variables.

Furthermore, few studies have systematically evaluated the spatial uncertainty of these data-driven models, particularly in regions with sparse training data or complex topography. Existing research predominantly assesses model performance solely based on overall accuracy metrics, which are inadequate for comprehensively capturing error distributions across heterogeneous landscapes. Consequently, the spatial representativeness of these estimation models remains largely unquantified, rendering them prone to site specificity and limited transferability when extrapolated to environmental conditions dissimilar to the training data. In the absence of comprehensive independent validation data across large scales, the Area of Applicability (AOA), as an emerging spatial analysis tool, can serve as a critical metric for quantifying spatial uncertainty and identifying valid prediction domains. The efficacy of AOA has been demonstrated in delineating reliable spatial prediction extents for diverse geophysical variables, including soil properties, Soil Moisture and LST (Lezama Valdes et al., 2021; Yu et al., 2025; Žížala et al., 2022).

To address these issues, we propose HyTC-TaNet, a hybrid Transformer-based deep learning architecture designed to integrate multi-day time series data for high-precision air temperature estimation, complemented by an AOA analysis to explicitly quantify spatial uncertainty. The specific objectives of this study are to:

(1) develop the HyTC-TaNet model integrating multi-day temporal information;

(2) quantify the contribution of temporal features and determine the physically optimal

sequence length;

(3) apply HyTC-TaNet to generate Ta at a 1 km spatial resolution and assess the spatial representativeness of the model through the AOA metric.

2. Materials

2.1 Study area

This study selects the middle and lower reaches of the Yangtze River in China, including Jiangsu, Anhui, and Hubei provinces, as the study area (108°21′E -121°57′E, 29°05′N to 35°20′N) (Fig. 1). Located in the middle latitude subtropical humid monsoon climate zone, this area exhibits pronounced spatial heterogeneity in geography, climate, and surface characteristics. The terrain gradually transitions from low-lying plains in the east to higher elevations in the central and western parts. The eastern part is dominated by the Yangtze River Basin plain, including the famous Jiang-Huai Plain, characterized by flat topography and a humid climate. The central region features hilly terrain and a transitional climate, primarily influenced by the Dabie Mountains, which lie along the Anhui-Hubei boundary and display distinct climatic gradients. The western section consists mainly of high mountains and rugged landscapes, such as the Wuling Mountains bordering Hubei and Hunan provinces, where climatic conditions are strongly shaped by topography. Overall, these three provinces encompass diverse landforms and climate types ranging from typical plains to mountainous environments, resulting in substantial spatial temperature variability. Therefore, this region provides a representative and valuable setting for temperature estimation studies.

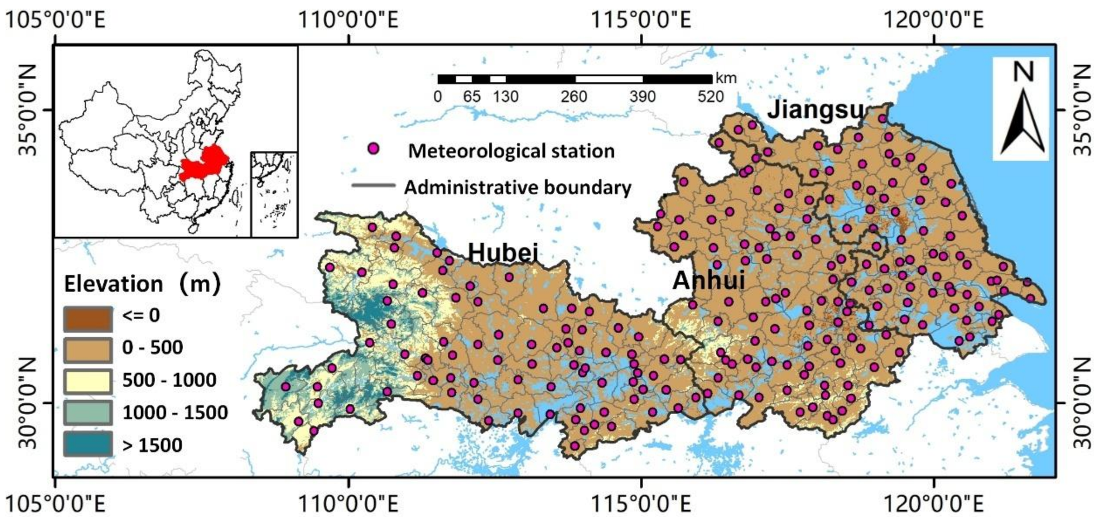

Fig. 1. Study area and locations of meteorological stations overlaid on a digital elevation model (DEM) background. The DEM data were obtained from the Shuttle Radar Topography Mission (SRTM).

2.2 Data collection and pre-processing

2.2.1 Meteorological station data

The air temperature meteorological station data used in this study are primarily sourced from the National Meteorological Science Data Center (http://data.cma.cn/). A total of 231 meteorological stations distributed across the study area were used, as shown in Fig. 1. After removing invalid and missing records, Ta data from 2003 to 2018 were used to develop, calibrate, and validate the proposed methods. In addition, the geographical attributes including longitude (LON), latitude (LAT), and elevation (DEM) were incorporated as spatial variables, while the day of year (DOY) was included as a temporal factor to account for seasonal effects.

2.2.2 Remotely sensed data

The remotely sensed data used in this study include LST, land cover (LC), Enhanced Vegetation Index 2 (EVI2), precipitation (GPM), soil moisture (SM), and solar radiation (SR).

LST: The LST data (hereafter referred to as TRIMS-LST) were produced by Zhang et al. (2021) and Tang et al. (2024). TRIMS-LST is an all-weather land surface temperature dataset that includes four types of LST: Terra-day (LSTTD), Terra-night (LSTTN), Aqua-day (LSTAD), and Aqua-night (LSTAN). The dataset features high image quality and seamless spatial continuity, with a spatial resolution of 1 km and a temporal frequency of four observations per day covering the time span from 2000 to 2023. Validation based on ground station data shows an mean bias error (MBE) of -2.26K to 1.73K, and a root mean square error (RMSE) ranging from 0.80K to 3.68K (Tang et al., 2024; Zhang et al., 2021).

Land Cover: The MODIS land cover type product (MCD12Q1) for the period 2003-2018 was used, which is available from the NASA Earthdata portal. To better assess the impact of land cover on daily mean temperature estimation, the original land cover types were reclassified into six categories: water, forest, shrubland, cropland, urban, and barren. The pixel values in the reclassified TIFF file range from [1, 6] in ascending order.

Enhanced Vegetation Index 2 (EVI2): The EVI2 dataset was derived from the author's previous work (Liu et al., 2020), based on surface reflectance products from Terra and Aqua satellites (MOD09A1 and MYD09A1), available through NASA's Level-1 and Atmosphere Archive and Distribution System (LAADS, https://ladsweb.nascom.nasa.gov/). Compared to standard operational EVI2 products derived from single sensors, this dataset employs a dual-sensor fusion strategy combined with an optimized cloud removal algorithm, which significantly enhances spatiotemporal continuity and effective pixel availability in cloud-prone regions. The processing workflow included sub-dataset extraction, image mosaicking, EVI2 calculation, data quality flagging, cloud pixel removal, replacement, interpolation, and curve filtering smoothing. The EVI2 calculation formula is as follows:

$$\mathrm{EVI2} = 2.5 \times \frac{\rho_{858} - \rho_{645}}{\rho_{858} + 2.4 \times \rho_{645} + 1}$$

Where ρ_{654} and ρ_{858} represent the reflectance of the first and second bands of the MOD09A1/MYD09A1 products, respectively.

Solar Radiation: The downward shortwave radiation data were sourced from the China Meteorological Forcing Dataset (CMFD)(He et al., 2020; Yang et al., 2010), and the data can be downloaded from the National Tibetan Plateau Scientific Data Center (http://data.tpdc.ac.cn/zh-hans/data/8028b944-daaa-4511-8769-965612652c49/). The CMFD integrates multiple reanalysis products, including Princeton University's Global Land Surface Model Data, Global Land Data Assimilation System (GLDAS), Global Energy and Water Exchanges-Surface Radiation Budget (GEWEX-SRB), and Tropical Rainfall Measuring Mission (TRMM), integrated with routine meteorological observation data from the China Meteorological Administration.

Precipitation: Precipitation data were obtained from the Global Precipitation Measurement (GPM)mission. The daily precipitation product used in this study is the Version 6 Level-3 IMERG Final Run product , which can be obtained from the Goddard Earth Sciences Data and Information Services Center Distributed Active Archive Center (GES DISC DAAC) website of the National

Aeronautics and Space Administration (NASA) (https://disc.gsfc.nasa.gov/datasets/GPM_3IMERGDF_06/summary).

Soil Moisture: The soil moisture data were obtained from the "China 1 km Resolution Daily All-Weather Surface Soil Moisture Dataset (2003-2019)" (Song et al., 2022), available from the National Tibetan Plateau Third Pole Environment Data Center (TPDC). This dataset was generated using 36 km resolution brightness temperature data from the AMSR-E and AMSR-2 passive microwave radiometers through downscaling and inversion processes.

All meteorological, geographic, temporal, and remote sensing variables used in this study are summarized in Table 1. Following batch preprocessing, all remote sensing datasets were reprojected to a uniform g geographic coordinate system. To ensure consistency, raster data (LC, DEM, LAT, LON, EVI2, SR and GPM) were resampled to a spatial resolution of 1 km × 1 km using the nearest-neighbor interpolation method. The meteorological station observations were then spatially matched with the corresponding raster data. Because satellite-derived products may contain missing values due to cloud contamination or sensor errors, data screening was conducted to remove invalid observations. Finally, a total of 380,750 paired samples comprising Ta and the corresponding predictor variables were generated for the period 2003-2018. The data were divided into three subsets: 2003-2012 for training, 2013-2015 for validation, and 2016-2018 for testing.

Table 1. Parameters used in this study and their abbreviations.

Abbreviation	**Predictor Variable**	**Data**	**Temporal Resolution**	**Spatial Resolution**	**Source**
Ta	Daily mean air temperature	Ground observations	Daily	--	Nation Meteorological Science Data Center
LST	Land surface temperature	TRIMS-LST	4 times per daily	1km	National Tibetan Plateau Data Center
LC	Land cover	MCD12Q1	1 year	500m	NASA-LAADS DAAC[1]
DEM/LON/LAT	Elevation/Longitude /Latitude	Digital elevation model	--	90m	Shuttle Radar Topography Mission (SRTM)
EVI2	Enhanced Vegetation Index 2	MO[Y]D09A1 Reflectance	8 days	500m	NASA-LAADS DAAC
SR	Solar radiation	CMFD	8 days	0.1°	National Tibetan Plateau Data Center
GPM	Precipitation	GPM_3IMERGDF	Daily	0.1°	NASA-GES DISC DACC[2]

SM	Soil moisture	Surface soil moisture data	Daily	1km	National Tibetan Plateau Data Center
DOY	Day of year		--	--	--

NASA-LAADS DAAC [1]: NASA Land Atmosphere Near Real-time Capability for EOS Data Active Archive Center

NASA-GES DISC DAAC [2]: NASA Goddard Earth Sciences Data and Information Services Center Distributed Active Archive Center

3. Methodology

Fig. 2 illustrates the overall workflow of this study. First, systematic preprocessing of the raw datasets was conducted, including spatial resolution harmonization and data normalization (see Section 2.2 for details). These preprocessing steps ensured data quality and consistency, providing a reliable foundation for subsequent analyses. Second, fifteen time-series datasets with varying temporal spans were constructed and used as inputs for air temperature estimation. We then conducted a systematic comparison between the proposed HyTC-TaNet model and several other hybrid deep learning models and traditional machine learning algorithms. Subsequently, Ta distribution maps were generated using the HyTC-TaNet model and compared against reference Ta product. These visualizations were used to illustrate the spatial performance of the model driven by the optimal temporal inputs and to examine the consistency between the estimated and reference temperature fields. Finally, we performed a comprehensive evaluation by analyzing feature importance via the SHapley Additive exPlanations (SHAP) method and providing a physical interpretation of the optimal temporal sequence, followed by an assessment of AOA to demarcate reliable monitoring regions.

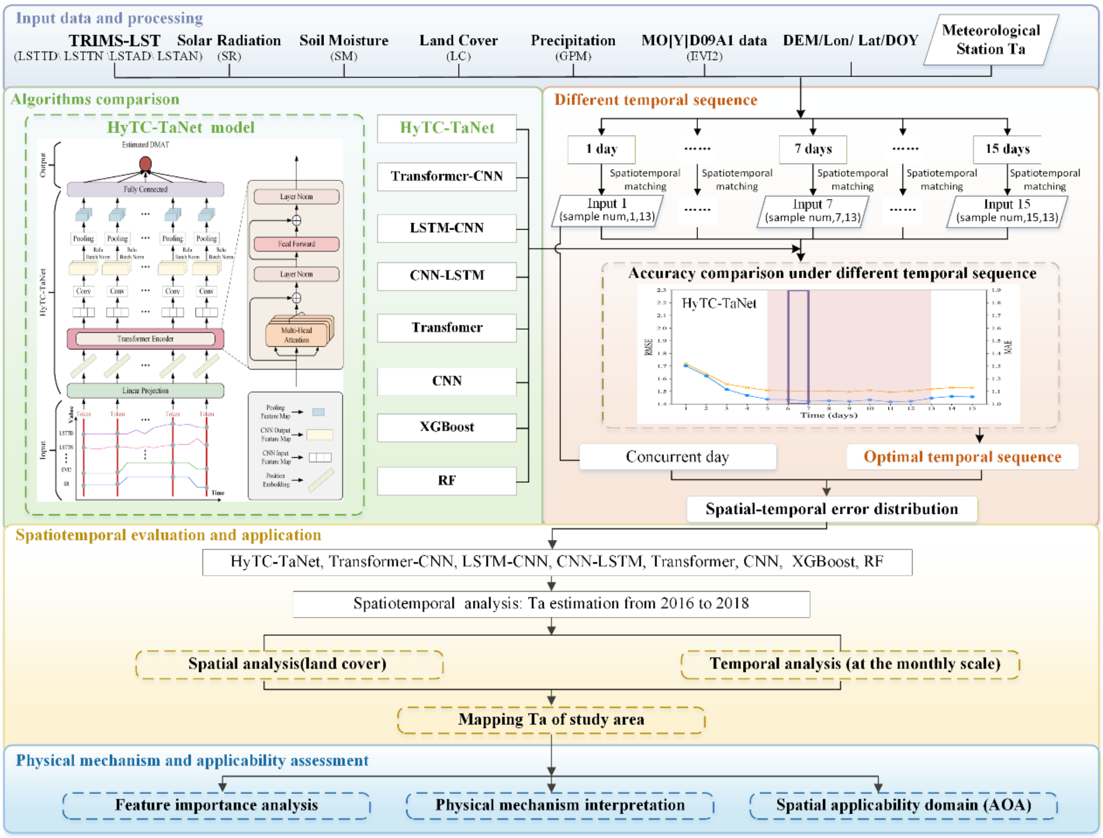

Fig. 2. The overall workflow of this study.

3.1 Time series input

To assess the impact of different temporal sequence lengths on the performance of air temperature estimation models, fifteen datasets with different temporal spans were constructed. Let $x_t \in R^D$ represent the feature vector at time step t, containing $D = 13$ distinct variables (including LST, SR, SM, etc.). For a specific temporal sequence length L, the model input $X_t^{(L)}$ used to predict Ta at time t is formulated as a sequence of historical feature vectors:

$$X_t^{(L)} = [x_{t-L+1}, x_{t-L+2}, \cdots, x_t]$$

where L denotes the temporal sequence length, ranging from 1 to 15 days (i.e., $L \in \{1, 2, \cdots, 15\}$). Consequently, the shape of the input tensor for each experimental group is (N, L, 13), where N represents the sample size.

This range of L was designed to systematically examine how the amount of historical information available to the model changes with increasing sequence length. Theoretically, longer time series provide richer temporal context, enabling the model to capture long-term temperature trends and potentially improving accuracy. However, excessively long sequences may introduce information redundancy and increase the risk of overfitting. Therefore, the experiment aimed to identify the optimal L that balances information richness with model generalization.

To ensure that the temporal sequence length was isolated as the sole independent variable, strict experimental controls were applied. While the temporal dimension L varied, the sample size N and the target temperature values remained identical across all fifteen datasets. Furthermore, all datasets underwent uniform preprocessing and spatio-temporal matching workflows. This rigorous design guarantees that any observed differences in model performance can be attributed exclusively to the variation in temporal sequence length, thereby ensuring the reliability and fairness of the comparison.

3.2 Development of HyTC-TaNet

Accurate air temperature estimation relies on effectively extracting key information from time series data. While classic deep learning architectures, such as Long Short-Term Memory (LSTM) networks, are explicitly designed to model temporal dependencies, they may encounter difficulties in capturing complex long-term interactions efficiently or suffer from the vanishing gradient problem over extended sequences. These limitations can hinder their ability to fully exploit dynamic temporal characteristics for high-precision estimation. To overcome these limitations, a hybrid model (HyTC-TaNet) was developed in this study. The model integrates the Transformer self-attention mechanism with the local feature extraction advantages of Convolutional Neural Networks (CNNs) (Vaswani et al., 2017). This combination allows the model to capture both global dependencies and local dynamics within time series data, thereby improving the accuracy of air temperature estimation. The overall model architecture is shown in Fig. 3.

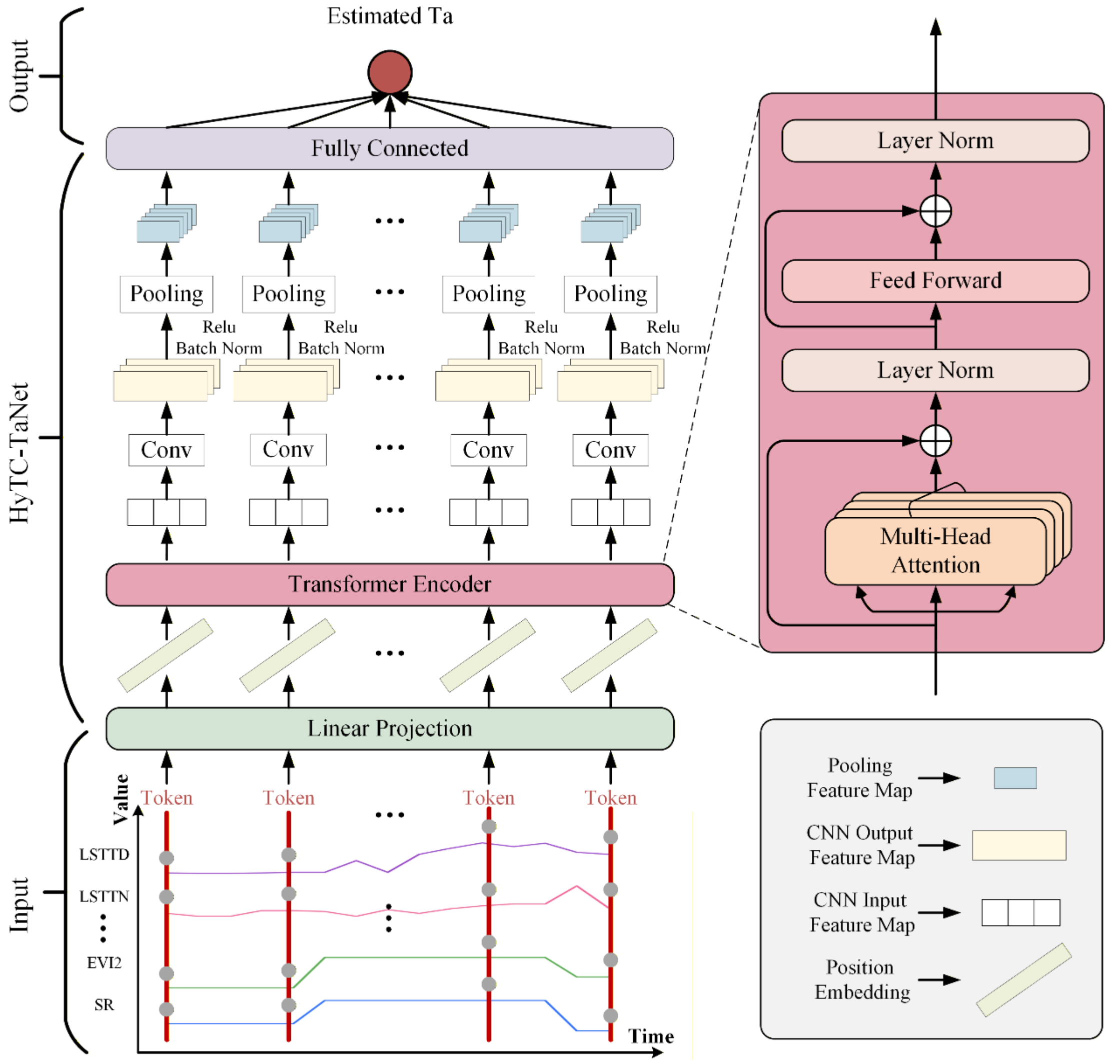

Fig. 3. The entire architecture of HyTC-TaNet.

The design of the HyTC-TaNet model fully considers the intrinsic characteristics of time series data. In the first stage, the model adopts a Transformer structure, which employs a self-attention mechanism to capture global dependencies within the time series. Unlike traditional models, the Transformer can dynamically adjust attention weights across the entire sequence, recognizing long-term dependencies and global information between time steps, which is crucial for capturing long-term trends and complex patterns in air temperature changes. Through this phase, the model can effectively learn global information within the time series.

To retain the order information of input sequences during parallel processing, the Transformer incorporates a positional encoding (PE) mechanism, which injects positional information into the input data. Specifically, positional encoding uses cosine and sine functions to encode each position in the sequence, allowing the model to parse the relative relationships between positions when processing the input sequence, thus ensuring that the model can leverage both the sequential information of the series and the advantages of parallel processing.

$$\mathrm{PE}\left(\mathrm{pos},\ 2i\right) = \sin\left(\frac{\mathrm{pos}}{10000^{2\mathrm{i/d\_model}}}\right)$$

$$\mathrm{PE}\left(\mathrm{pos},\ 2i+1\right) = \cos\left(\frac{\mathrm{pos}}{10000^{2\mathrm{i/d\_model}}}\right)$$

where, pos represents the position index, d_model denotes the dimensionality of the input features, and i refers to the feature dimension encoding, with a range of [0, d_model/2-1].

Subsequently, HyTC-TaNet introduces a one-dimensional Convolutional Neural Network (1D CNN) to further extract local features from the time series. The convolution operation efficiently captures dependencies between adjacent time steps, which are often difficult for traditional methods to address. By sliding convolutional kernels along the temporal dimension, the CNN module can effectively identify local patterns and short-term fluctuations within the time series, thus enhancing the model's ability to perceive local features.

To further accelerate the neural network training process and improve the model’s convergence speed and stability, a batch normalization layer (BatchNorm) is typically added. This layer helps alleviate the gradient vanishing problem during training and improves the model's generalization capability. The 1D CNN can be described as:

$$h[i] = \mathrm{relu}(\gamma\ (\frac{\sum_{j=0}^{\mathrm{k-1}} w[j] * x[i+j] + b - \mu}{\sqrt{\sigma^2 + \varepsilon}}) + \beta)$$

where h[i] is the i-th element of the output feature map, γ and $\beta$are learnable parameters, w[j] represents the weights of the convolution kernel, x[i+j] is the input sequence, bis the bias term, k is the size of the convolution kernel, μ is the mean of each feature channel, σ^2 is the variance of each feature channel, and ε is a small constant, typically set to 10^{-5}. 'relu' refers to the activation function, which is written as:

$$\mathrm{f(x)} = \begin{cases} x \ if \ x > 0 \\ 0 \ if \ x \le 0 \end{cases}$$

By integrating the complementary strengths of the Transformer and CNN architectures, the HyTC-TaNet model not only excels in global modeling but also enhances the ability to capture local dependencies. The model's structural design reflects a profound understanding of time series data, balancing the learning of long-term dependencies and local features, thus improving its performance in air temperature estimation tasks. Finally, through further processing via fully connected layers, HyTC-TaNet outputs the estimated air temperature values.

3.3 Other models used for comparison

3.1.1 Deep learning models

Models capable of handling time series datasets and extracting temporal information also include LSTM(Hochreiter and Schmidhuber, 1997). LSTM, as a special type of Recurrent Neural Network (RNN)(Elman, 1990), addresses the severe vanishing gradient problem faced by traditional RNNs when processing long sequence data by introducing a structure called the "memory cell." It has become an essential tool in sequence modeling. The core of the LSTM model lies in its unique gating mechanism, which includes the forget gate (Ft), input gate (It), and output gate (Ot). These gates, in conjunction with the memory cell, form the central structure of LSTM, controlling the flow and updating of information in the time series. Specifically, Ft determines the proportion of information to be forgotten from the previous hidden state (Ct-1), thereby controlling the model's retention of historical information. It governs the influence of current input information on the memory cell, determining the amount of current input information stored in the hidden state (Ct). Ot is responsible for selectively passing information from the internal state (Ct) to the output (ht), thereby generating the final output.

Therefore, we compare hybrid deep learning models such as LSTM-CNN (LC) and CNN-LSTM (CL). To further validate the effectiveness of our proposed HyTC-TaNet model, we also compared it with the CNN-Transformer (CT) hybrid deep learning model, as well as the standalone Transformer (T), CNN (C), and other models.

3.1.2 Traditional machine learning models

Extreme Gradient Boosting (XGBoost) Model: XGBoost is an ensemble algorithm based on Gradient Boosting Decision Trees (GBDT), specifically designed for regression and classification tasks(Chen and Guestrin, 2016). XGBoost iteratively constructs multiple weak learners (typically decision trees) and combines them into a strong learner by assigning weights to these weak models. In each iteration, a new weak learner is focused on fitting the residuals of the previous model, thereby progressively improving the overall performance of the model. Unlike traditional GBDT, XGBoost introduces a regularization term in the loss function to prevent overfitting.

Random Forest (RF) Model: RF is an ensemble learning algorithm used for regression and classification, introduced by Breiman (BREIMAN, 2001). The RF model makes predictions by constructing multiple decision trees and aggregating their results. The training of each decision tree is independent, and subsamples are randomly drawn from the original data for training. For regression tasks, the output of the RF model is the average or weighted average of the results from all decision trees. Due to its ensemble nature, RF has strong modeling capabilities and is effective in preventing overfitting.

3.4 SHAP for model interpretation

SHAP is an interpretable modelling technique based on game-theoretic Shapley values, used to quantify the contribution of each feature to the model's estimation results (Lundberg and Lee, 2017). By constructing an additive feature attribution model that satisfies theoretical properties such as consistency and local accuracy, SHAP can provide global or local explanations for any model. This interpretability framework has proven particularly valuable in meteorology and agricultural research for diagnosing complex models related to, for instance, evapotranspiration estimation and crop yield prediction (Liu et al., 2025a; Lu et al., 2025; Xu et al., 2025). In this study, we employ the GradientExplainer interpreter to explain the output of the HyTC-TaNet model with optimal temporal sequence data as input, generating feature importance summary plots and bee swarm plots to reveal the contribution, impact direction, and feature importance ranking of each input variable.

3.5 Area of Applicability

While DL models often exhibit superior performance in extracting non-linear patterns from meteorological data, their validity is strictly constrained by the representativeness of the training distribution. Standard cross-validation strategies (e.g., random k-fold) tend to overestimate model performance in geographically distinct regions where environmental conditions deviate significantly from the training domain (i.e., spatial extrapolation) (Roberts et al., 2017). To quantify the spatial generalization capability of the proposed model(Yu et al., 2025), we adopted the AOA methodology proposed by Meyer and Pebesma (2021) (Meyer and Pebesma, 2021).

The AOA method is implemented to rigorously delineate the model's valid prediction domain by quantifying the environmental similarity between prediction location and training stations in a multidimensional feature space, thereby explicitly identifying regions subject to extrapolation risks. The computation procedure begins with the construction of a physically-constrained feature space. Given the heterogeneity in physical units and the varying importance of predictor variables, the original feature matrix requires transformation. First, standardization is performed to eliminate unit differences using the Z-score method:

$$z_{i,j} = \frac{x_{i,j} - \mu_j}{\sigma_j}$$

where $z_{i,j}$ denotes the standardized value of the j-th feature at training location i (i.e., $X_{i,j}$); and μ_j and σ_j represent the mean and standard deviation of the j-th feature within the training dataset. Subsequently, to ensure the distance metric is driven by dominant physical factors (e.g., topography and thermal properties), a weighting scheme is applied to the standardized values. The final transformed feature value $x'_{i,j}$ is obtained as:

$$x'_{i,j} = w_j \cdot z_{i,j}$$

where w_j denotes the weight assigned to feature j. Based on this weighted feature space, the degree of environmental deviation for a target prediction location k is quantified by the Dissimilarity Index (DI). The calculation of DI involves determining the ratio between the distance to the nearest training sample and the internal compactness of the training domain. First, the Euclidean distance between a given prediction location k and a training location i in the feature space can be expressed as follows:

$$d(k,i) = \sqrt{\sum_{j=1}^{m} (x'_{k,j} - x'_{i,j})^2}$$

where m is the number of feature variables and d denotes the Euclidean distance. Next the minimal distance from the prediction location k to the set of training locations S is then given as follows:

$$d_k = \min_{i \in S}\big(d(k,i)\big)$$

The final DI for the prediction location k (i.e., DI_k) is defined as follows:

$$DI_k = \frac{d_k}{\bar{d}}$$

where $\bar{d}$ denotes the arithmetic mean of the Euclidean distances between each training station and its nearest neighbor in the feature space.

To differentiate between valid prediction areas ("Inside AOA") and extrapolation areas ("Outside AOA"), an adaptive threshold τ is determined. This threshold is derived via a Leave-One-Out Cross-Validation (LOOCV) procedure performed on the training dataset. In each iteration, a single training site is treated as a validation point, and its DI is evaluated relative to the remaining N-1 training sites. The applicability threshold is defined as the upper whisker of the distribution of these cross-validated DI values, following the standard outlier detection rule:

$$\tau = Q_3 + 1.5 \times IQR$$

where Q_3 represents the 75th percentile and IQR is the interquartile range of the cross-validated DI distribution. Consequently, prediction location exhibiting $DI_k > \tau$ are classified as being outside the area of applicability, indicating a statistically significant deviation from the environmental conditions covered by the training stations.

3.6 Evaluation metrics

To evaluate the performance of the model, we selected four commonly used statistical metrics: Root Mean Square Error (RMSE), Mean Absolute Error (MAE), the coefficient of determination (R^2) and residuals (e_i). Specifically, RMSE measures the square root of the difference between the estimated and observed values, effectively reflecting the magnitude of estimation errors while assigning higher weights to larger errors. This makes it commonly used to assess the accuracy of regression models. MAE calculates the average of the absolute differences between the estimated and observed values, providing a simple and intuitive measure of error, suitable for evaluating the average error level across all samples. The coefficient of determination (R^2) is used to assess the model's goodness of fit, representing the model's ability to explain the data, with values ranging from 0 to 1. The closer the R^2 value is to 1, the better the model fits the data. The residuals (e_i) are analyzed on a monthly scale to evaluate the model's temporal performance and identify seasonal biases. Through the comprehensive evaluation of these metrics, we are able to analyze the model's performance in terms of error, bias, and fit, thereby gaining a thorough understanding of its estimation capabilities.

$$\text{RMSE} = \sqrt{\frac{1}{n}\sum_{i=1}^{n}(y_i - \hat{y}_i)^2}$$

$$\text{MAE} = \frac{1}{n}\sum_{i=1}^{n}|y_i - \hat{y}_i|$$

$$R^2 = 1 - \frac{\sum_{i=1}^{n}(y_i - \hat{y}_i)^2}{\sum_{i=1}^{n}(y_i - \bar{y})^2}$$

$$e_i = y_i - \hat{y}_i$$

where y_i and $\hat{y}_i$ represent the observed values and the model's estimated values, respectively, $\bar{y}$ denotes the mean of the actual values, and n represents the sample size.

4. Results

4.1 Analysis of optimal temporal sequence

Fig. 4 illustrates the variation of RMSE and MAE with temporal sequence length for HyTC-TaNet and other models. The RMSE and MAE curves of all models exhibit a similar pattern, with errors decreasing rapidly at first, reaching their lowest values around 6-7 days, maintaining a relatively stable minimum range, and then showing a slight increase or leveling off as the temporal sequence becomes longer. This trend indicates that the performance of air temperature estimation models is influenced by temporal sequence length; however, longer sequences do not necessarily lead to improved estimation accuracy and may also increase computational costs, thereby reducing model training efficiency.

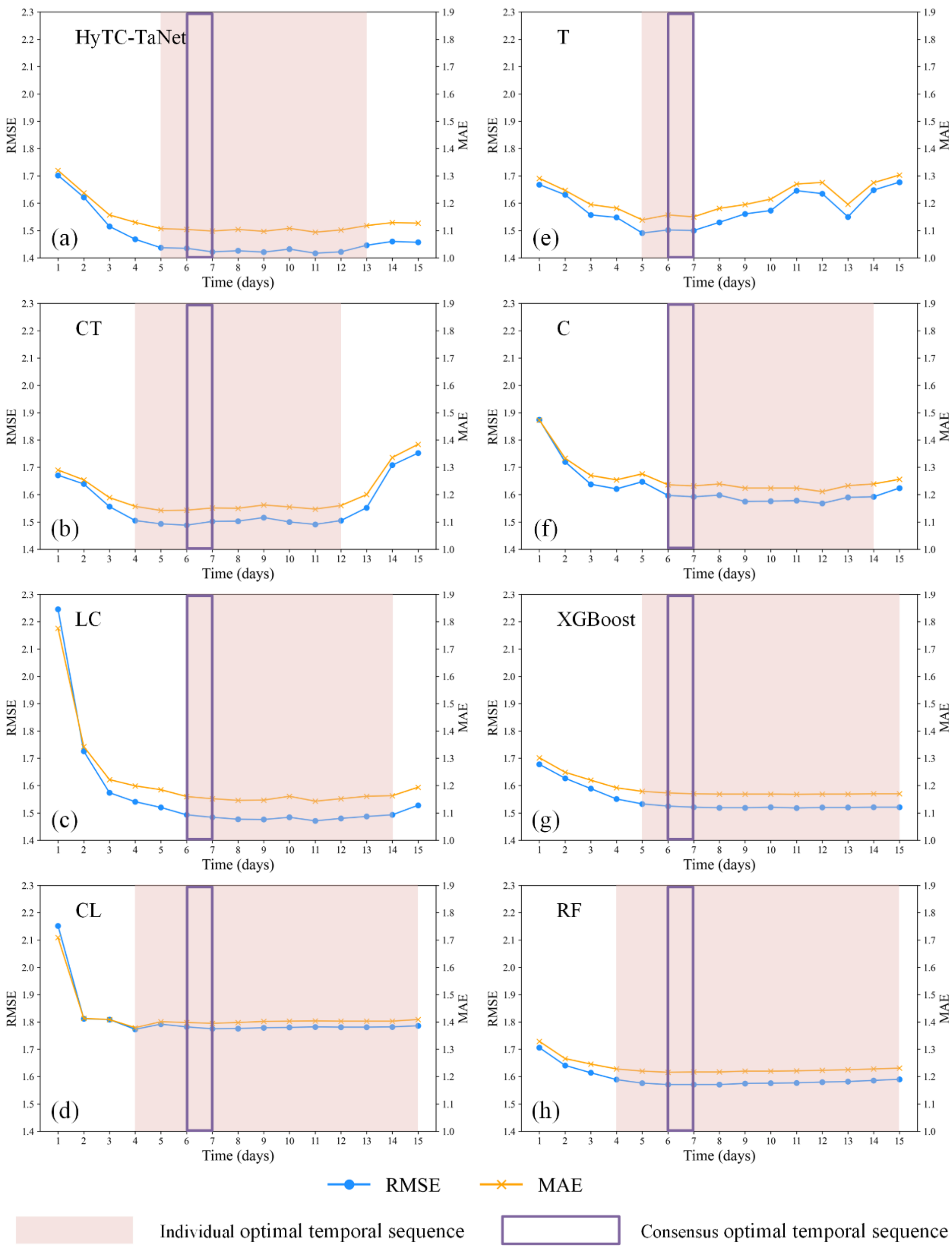

Fig. 4. Variation of RMSE and MAE with temporal sequence length for HyTC-TaNet and other models.

Overall, HyTC-TaNet consistently achieves lower RMSE values than all other models across most temporal sequence settings, except for the concurrent daily sequence, and also exhibits greater stability relative to other deep learning models. The minimum points of HyTC-TaNet (ours), CT, LC, CL, T, C, XGBoost, and RF are respectively located at the x^{11th}, x^{6th}, x^{4th}, x^{9th}, x^{7th}, x^{12th}, x^{10th}, and x^{7th} days (Table 2). Among the results, the HyTC-TaNet model achieved an RMSE of 1.417°C, which is 7.5% lower than that of the LC model (1.531°C), and an MAE of 1.094°C, representing a 7.8% improvement over LC (1.186°C). Its coefficient of determination (R^2 = 0.976) was also the highest among all models, indicating superior overall accuracy and robustness.

Table 2. Minimum points and performance metrics (RMSE, MAE, and R^2) for all models.

Model	Minimum points (days)	RMSE	MAE	R^2
HyTC-TaNet (ours)	x^{11th}	**1.417**	**1.094**	**0.976**
CT	x^{6th}	1.488	1.143	0.974
LC	x^{4th}	1.531	1.186	0.972
CL	x^{9th}	1.605	1.249	0.969
T	x^{7th}	1.500	1.150	0.973
C	x^{12th}	1.568	1.211	0.971
XGBoost	x^{10th}	1.502	1.156	0.973
RF	x^{7th}	1.538	1.191	0.972

This study conducted a comparative analysis based on the air temperature estimation results from six DL models and two ML models. To identify the individual optimal temporal sequence, a threshold criterion was established: the sequence should be a continuous period around the time point of minimum RMSE, within which all RMSE did not exceed the minimum by more than 0.03. Based on this criterion, we determined the individual optimal temporal sequences for each model, as detailed in Fig. 4. Across 15 time series inputs, the best estimation results for each model did not always occur at a specific sequence length. The individual optimal temporal sequences for HyTC-TaNet (ours), CT, LC, CL, T, C, XGBoost, and RF are 5-13 days, 4-12 days, 6-14 days, 4-15 days. 5-7 days, 6-14 days, 5-15 days, and 4-15 days, respectively. The consensus optimal temporal sequence for air temperature estimation, defined as the intersection of all model-specific individual optimal temporal sequence, was determined to be 6-7 days. This period represents the most reliable timeframe for air temperature estimation, as all models consistently perform within the defined RMSE threshold here. Even within this period of consensus optimal temporal sequence, HyTC-TaNet(ours) achieved the lowest mean RMSE (1.429°C), lowest mean MAE (1.101°C) and highest R^2 (0.976), edging out the LC model (1.548°C, 1.206°C and 0.972). This underscores the superior precision of HyTC-TaNet under consensus optimal temporal sequence.

These results suggest that HyTC-TaNet achieves the best overall performance and a strong capability in capturing temporal dynamics. Furthermore, the performance of HyTC-TaNet exceeded that of the CT model, and the LC model also outperformed the CL model. This further indicates that placing the model specifically designed to extract temporal information at the front of a cascading structure is more advantageous for precise air temperature estimation.

4.2 Spatial-temporal error distribution

This section validates the optimal estimation temporal sequence using station-level MAE statistics. The test set contains a total of 78 meteorological stations. The percentages of meteorological stations with an MAE below 1.4 °C for all models, based on the concurrent day and 7-day time series inputs, are shown in Fig. 5. Compared with the concurrent day data, all models exhibited substantial reductions in MAE when using the 7-day time series. Specifically, for the HyTC-TaNet model, 82% of the stations had an MAE less than 1.4°C with the concurrent day data, increasing to 96% with the 7-day time series. For the CT model, the corresponding percentages were 82 % and 91 %, respectively. The LC model showed a dramatic improvement from only 4 % of stations below 1.4 °C with concurrent day input to 92 % with the 7-day input. In contrast, the CL model showed no stations below 1.4 °C on the concurrent day, but 55 % fell below that threshold when using the 7-day sequence. Among traditional machine learning models, XGBoost improved from 78 % to 92 %, and RF from 74 % to 90 % between the concurrent day and 7-day inputs. These results consistently demonstrate that incorporating temporal information markedly enhances model performance across all approaches. Fig. 6 further illustrates the spatial distribution of MAE across all meteorological stations on the concurrent day and 7-day time series data in detail, revealing spatially coherent reductions in estimation errors under the temporally extended inputs.

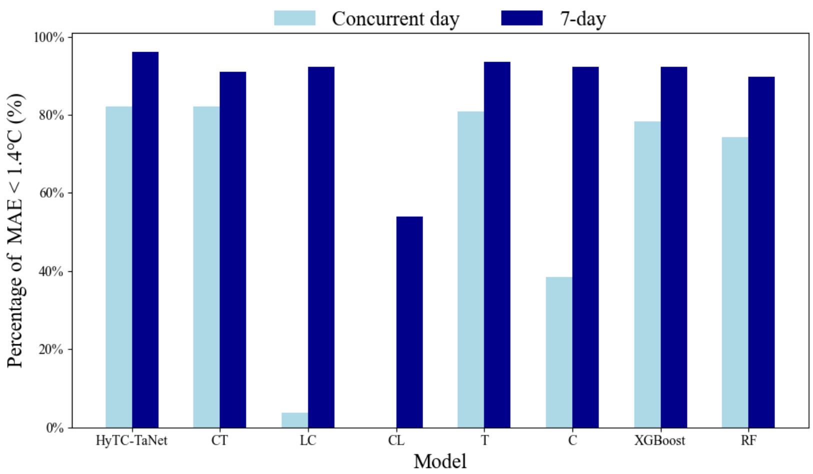

Fig. 5. Percentage of stations with an MAE less than 1.4°C for models on the concurrent day and 7-day time series data.

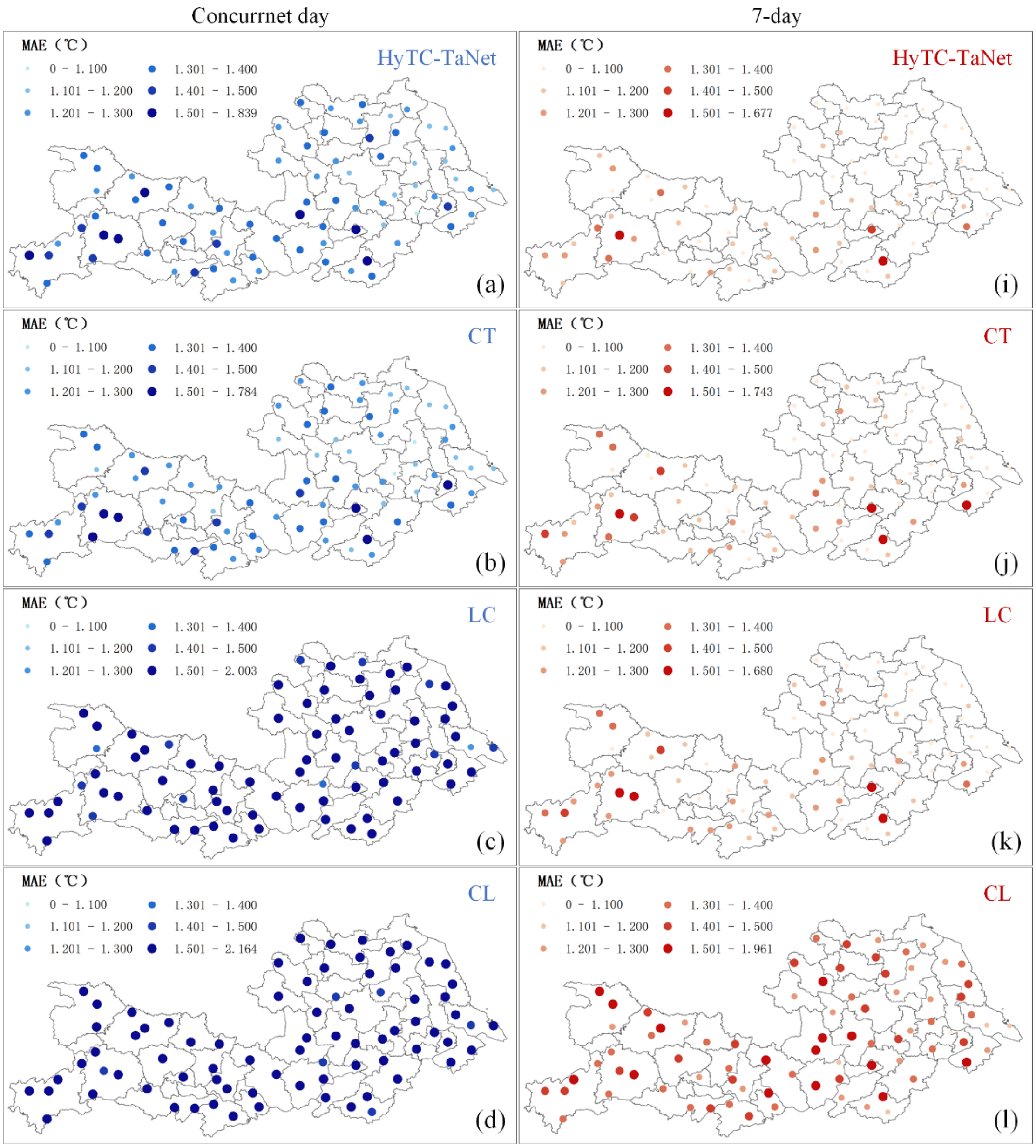
Concurrnet day
7-day
MAE（℃）
0 - 1.100
1.101 - 1.200
1.201 - 1.300
1.301 - 1.400
1.401 - 1.500
1.501 - 1.839
HyTC-TaNet
(a)
1.501 - 1.677
(i)
1.501 - 1.784
CT
(b)
1.501 - 1.743
(j)
1.501 - 2.003
LC
(c)
1.501 - 1.680
(k)
1.501 - 2.164
CL
(d)
1.501 - 1.961
(l)

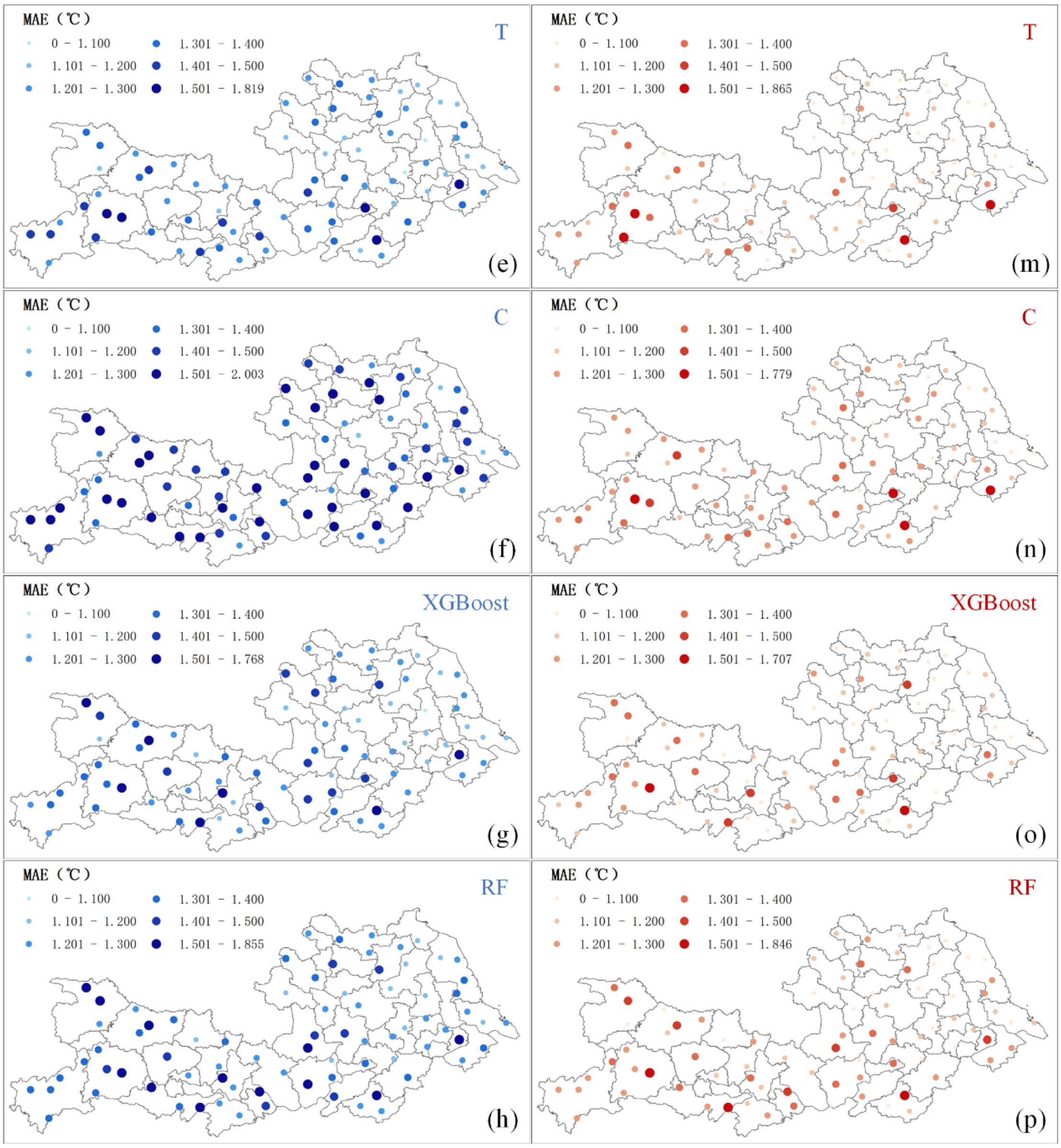

Fig. 6. Spatial distribution of MAE values for all models. (a)-(h) represent the MAE for all models on the concurrent day data. (i)-(p) represent the MAE for all models on the 7-day time series data.

4.3 Spatial performance evaluation of all models

Previous studies have shown that land cover type significantly influences the relationship between LST and air temperature (Lin et al., 2012; Marzban et al., 2018). To further assess this effect, we calculated the MAE for different land cover types and compared the performance of all model. As shown in Fig. 7, in areas characterized by complex surface dynamics including urban, cropland, and shrubland, all models exhibited markedly lower MAE values when using the 7-day time series input compared with the concurrent day data. Under the concurrent day setting, the CT model had the lowest MAE value; however, when the temporal sequence was extended to seven days, the HyTC-TaNet model yielded the best overall performance, recording the lowest MAE among all models.

In contrast, for water bodies and barren lands, the machine learning models outperformed the deep learning models. A straightforward explanation might attribute this to the limited sample size of these land cover types (1.1% and 1.3% of the total dataset, respectively), which could constrain deep learning models' capacity for effective feature learning in these regions. It is plausible that the inherent physical simplicity of these surfaces does not require such complex mapping, making simpler models a more robust choice for the conditions examined in this study; however, the generalizability of this principle must be tested with alternative data sources and across different geographical domains. Additionally, in the urban, crop, and bushes types, on the concurrent day time series data, the CL model outperformed the LC model; whereas on the 7-day time series data, the LC model exhibited better performance compared to the CL model. This indicates that placing the model specifically designed for temporal information extraction at the front of a cascading structure also enhances generalization ability and adaptability under spatial heterogeneity.

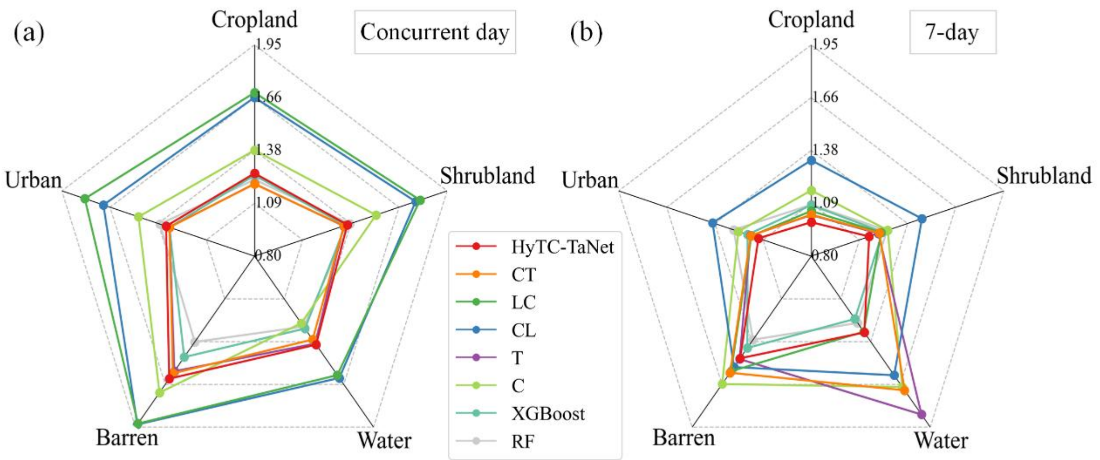

Fig. 7 Radar chart of MAE values for different land cover types. (a) concurrent day data, (b) 7-day time series data.

4.4 Comparative monthly performance of all models

For the temporal analysis, this study focuses on the monthly distribution of residuals between the estimated and observed Ta. Fig. 8 presents box plots of the residuals aggregated by month for each model. It is evident that, compared to the concurrent day input, utilizing a 7-day time series input substantially enhances the stability of all models, as reflected in the reduced fluctuation amplitude of residuals for each month. With the concurrent day input, the medium of residual values for XGBoost and RF models are significantly lower than 0°C from January to December, indicating that these two machine learning methods tend to underestimate the Ta in all months. However, with the 7-day time series input, the medium of residual values for XGBoost and RF models approach 0°C, especially in July and August. The experimental results suggest that, compared to traditional models based on the concurrent day input, introducing more time series data effectively reduces the underestimation of air temperature. The HyTC-TaNet and CT models exhibit a narrower fluctuation range in the median of residual values across months compared to the LC, CL, XGBoost, and RF models under both input settings. Whereas the CT model shows a narrower fluctuation range in the median of residual values with the concurrent-day data, the HyTC-TaNet (ours) model achieves the minimal variation and thus the highest stability when using the 7-day time series input.

By analyzing the monthly MAE values of all models on different input settings, it is clear that, compared to the concurrent day input, the monthly MAE of all models with the 7-day time series input is significantly reduced (Fig. 9). Furthermore, with the concurrent day input, the difference between the monthly maximum and minimum MAE for the HyTC-TaNet model is 0.488°C, which is the lowest among all models, and 0.677°C lower than the difference for the LC model. When using 7-day time series input, the monthly MAE of the HyTC-TaNet model is consistently lower than that of all other models in all months except for March, July and August. Notably, the range of the LC model's monthly MAE decreased by 0.61°C when shifting from the concurrent day to the 7-day time series input. Moreover, with the 7-day time series input, the monthly MAE of the LC model is consistently lower than that of the CL model. This indicates that placing the model specifically designed for temporal information extraction at the front of a cascading structure also enhances estimation accuracy across different months with minimal performance fluctuation.

563

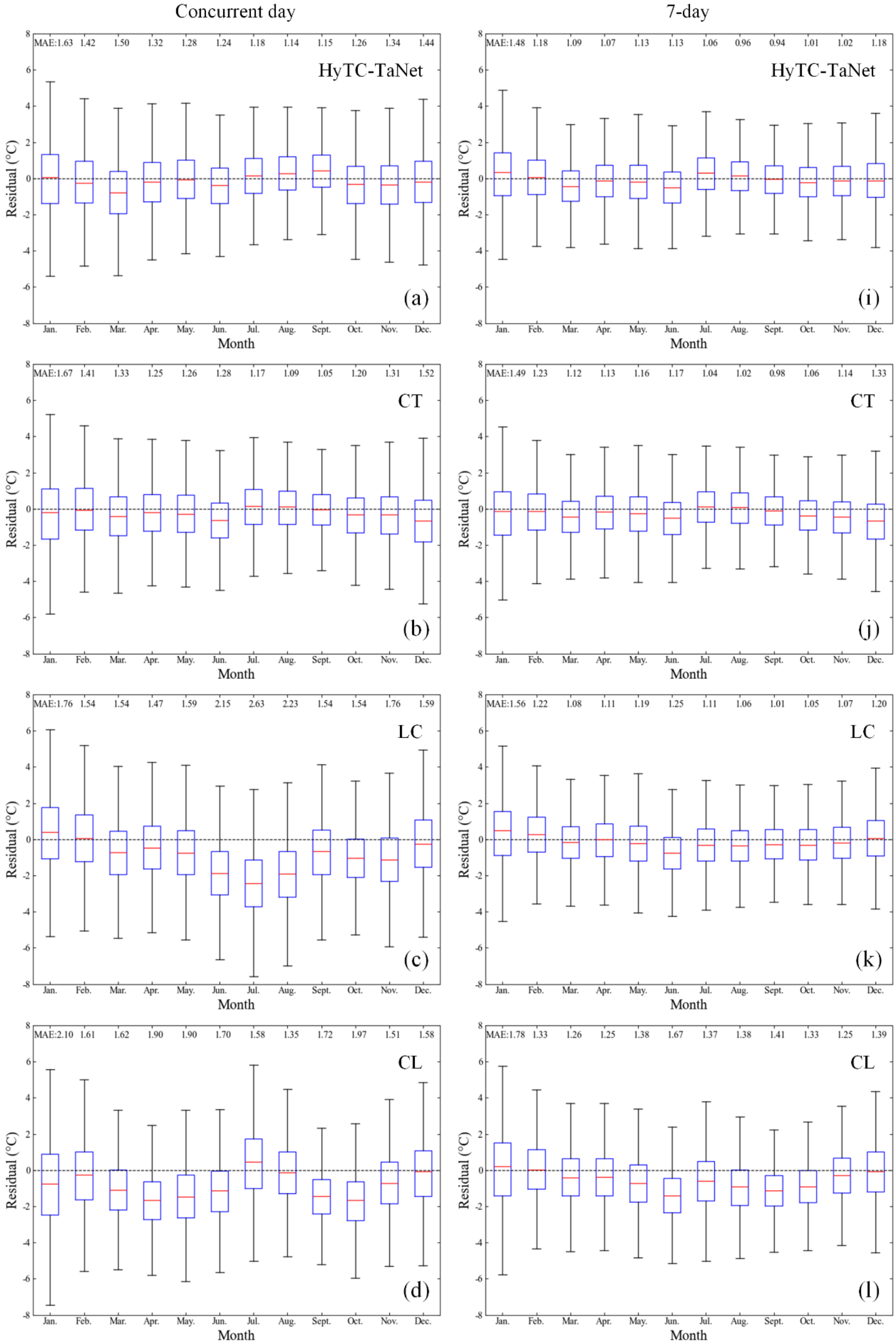

Concurrent day
7-day
MAE:1.63 1.42 1.50 1.32 1.28 1.24 1.18 1.14 1.15 1.26 1.34 1.44
HyTC-TaNet
(a)
MAE:1.48 1.18 1.09 1.07 1.13 1.13 1.06 0.96 0.94 1.01 1.02 1.18
(i)
MAE:1.67 1.41 1.33 1.25 1.26 1.28 1.17 1.09 1.05 1.20 1.31 1.52
CT
(b)
MAE:1.49 1.23 1.12 1.13 1.16 1.17 1.04 1.02 0.98 1.06 1.14 1.33
(j)
MAE:1.76 1.54 1.54 1.47 1.59 2.15 2.63 2.23 1.54 1.54 1.76 1.59
LC
(c)
MAE:1.56 1.22 1.08 1.11 1.19 1.25 1.11 1.06 1.01 1.05 1.07 1.20
(k)
MAE:2.10 1.61 1.62 1.90 1.90 1.70 1.58 1.35 1.72 1.97 1.51 1.58
CL
(d)
MAE:1.78 1.33 1.26 1.25 1.38 1.67 1.37 1.38 1.41 1.33 1.25 1.39
(l)
Residual (°C)
Month
Jan. Feb. Mar. Apr. May. Jun. Jul. Aug. Sept. Oct. Nov. Dec.

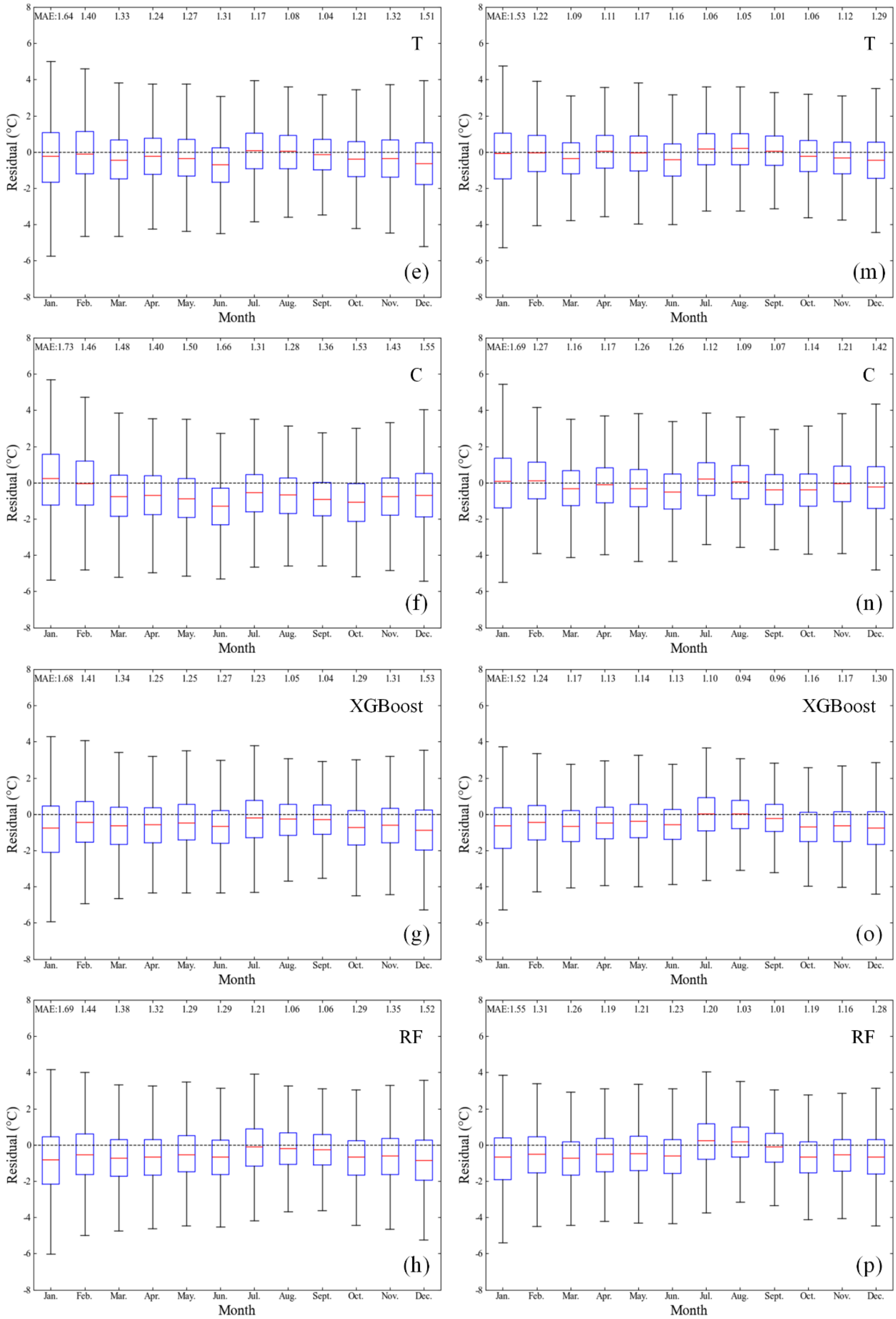

Fig. 8. The monthly distribution of residuals for each model. Box plots of residuals for all months. Panels (a)-(h) correspond to models using the concurrent day input, while panels (i)-(p) correspond

to models using the 7-day time-series input.

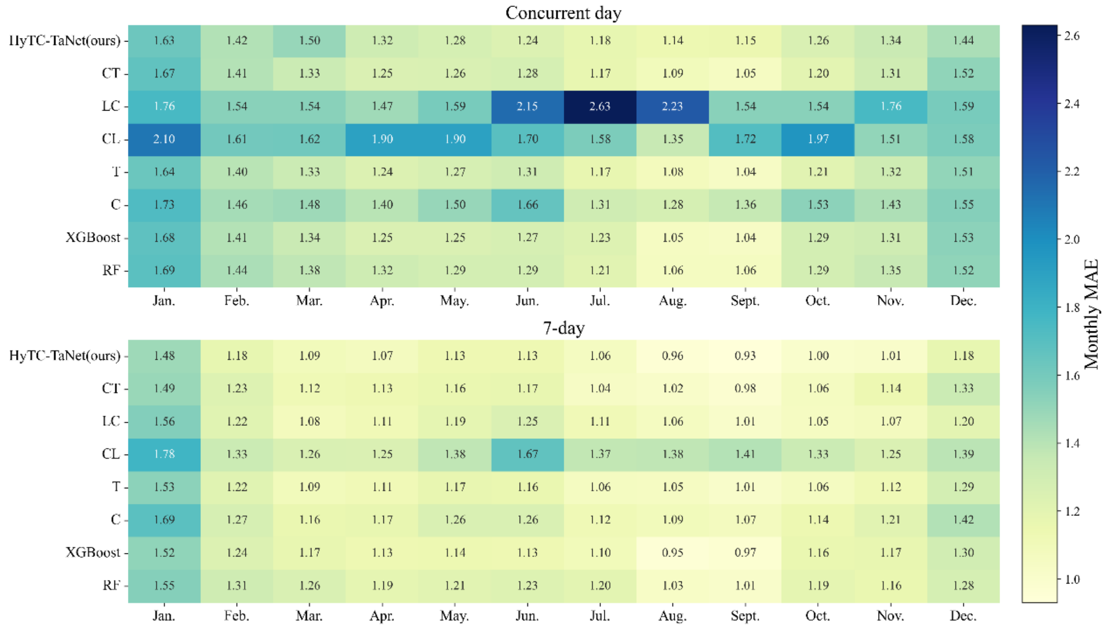

Fig. 9. Visualization of monthly MAE for all models under concurrent day (top) and 7-day (bottom) input settings.

4.5 Spatial and temporal distribution of Ta

Fig. 10 shows the spatiotemporal distribution of the Ta estimated by our proposed HyTC-TaNet model using the 7-day time series data (b1-b4) and the Ta product published by Zhao et al.(a1-a4)(Zhao et al., 2025). The selected dates represent different seasons: January 15 (a1-d1) for winter, April 15 (a2-d2) for spring, July 15 (a3-d3) for summer, and November 15 (a4-d4) for autumn. Overall, the spatial patterns of the two datasets exhibit strong similarity and clear elevation dependence. In particular, both show markedly lower temperatures in the high-altitude regions of western and central parts of the study area, consistent with established climatic and topographic gradients.

Despite the general agreement, the HyTC-TaNet results display enhanced capability in resolving fine-scale spatial details. As shown in areas such as the Yangtze River Basin, the boundary between Anhui and Hubei provinces, and the northern part of Anhui and Jiangsu provinces, Fig. 10(d1) highlights finer spatial variations associated with water bodies and their surrounding landscapes. Compared with the reference Ta product, our estimated results exhibit more pronounced gradient changes along water-land boundaries and provide a clearer delineation of small-scale tributaries and lakes, reflecting surface heterogeneity more faithfully. In contrast, the reference Ta product appears relatively smooth in these local areas, with some water bodies and boundary transition information not explicitly captured. These findings confirm that the proposed HyTC-TaNet method substantially improves the spatial fidelity of Ta fields. By effectively recovering fine-scale texture information that is often smoothed out in traditional products, the model demonstrates superior capability in capturing complex surface thermal patterns, particularly over heterogeneous landscapes and transitional zones.

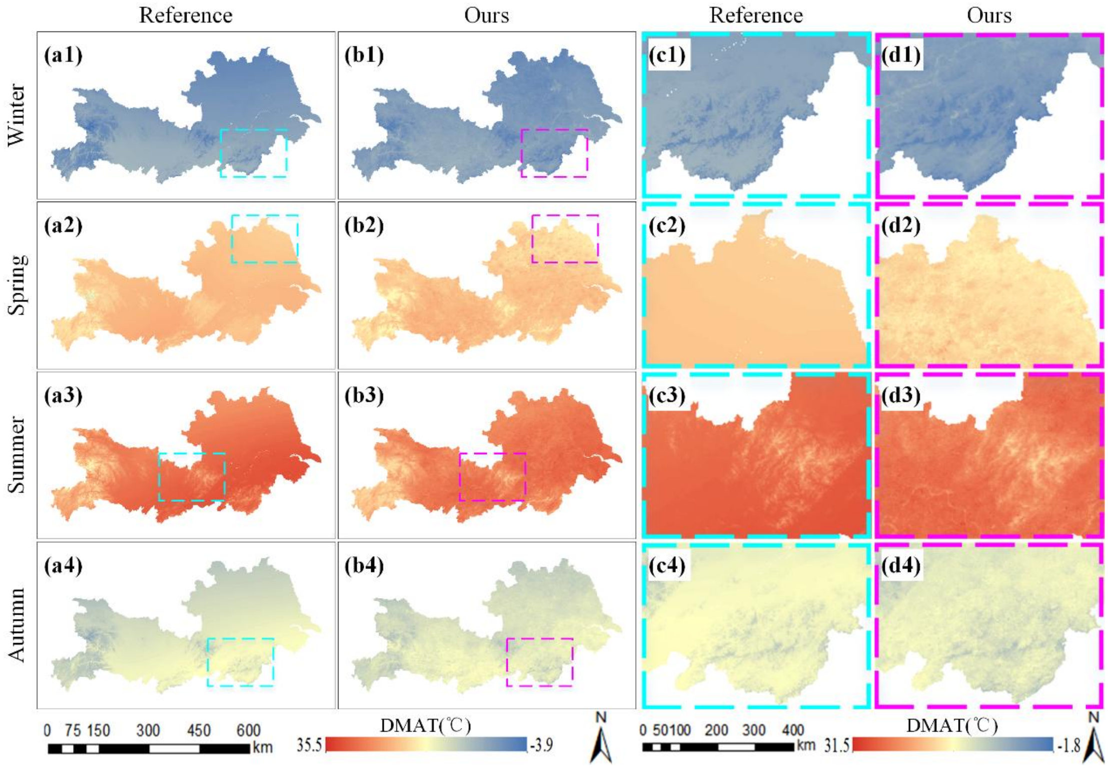

Fig. 10. Spatial and temporal distribution of Ta estimated by the proposed HyTC-TaNet model (b1-b4) and the reference Ta product of Zhao et al (2025) across four seasons: (a1) - (d1) winter, (a2) - (d2) spring, (a3) - (d3) summer, and (a4) - (d4) autumn.

5. Discussion

5.1 Analysis of feature importance using SHAP

To quantify the contribution of each input variable to air temperature estimation, we applied SHAP to the HyTC-TaNet model using the 7-day time-series input. Feature importance was derived from the mean absolute SHAP values, while the direction and strength of each feature's effect were visualized using summary and bee-swarm plots (Fig. 11).

As shown in Fig. 11(a), the ranking of mean absolute SHAP values reveals that solar radiation (SR) exerts the greatest overall influence on model outputs, followed by LSTTN and LSTAN. The bee swarm plot in Fig. 11(b) further illustrates the specific impact direction and strength of each feature on the model's estimation. It is clear that the SHAP values of SR have the widest distribution, indicating its strongest influence on the model's estimation. Higher SR values correspond to positive SHAP values, suggesting a positive contribution to air temperature, whereas lower SR values lead to negative SHAP values, resulting in underestimation of Ta. The impact directions of the four LST features are consistent with SR. In contrast, the features SM, GPM, DEM, LC, and EVI2 exhibit negative correlations with air temperature, whereby higher feature values are associated with lower estimated Ta. These findings are consistent with established meteorological and surface energy-balance principles: higher SR and LST correspond to warmer surface and air conditions, while increased soil moisture or precipitation suppresses heating through enhanced latent heat flux. The agreement between model-learned feature effects and physical processes indicates that HyTC-TaNet successfully captures meaningful environmental interactions, providing both strong predictive capability and interpretable physical realism.

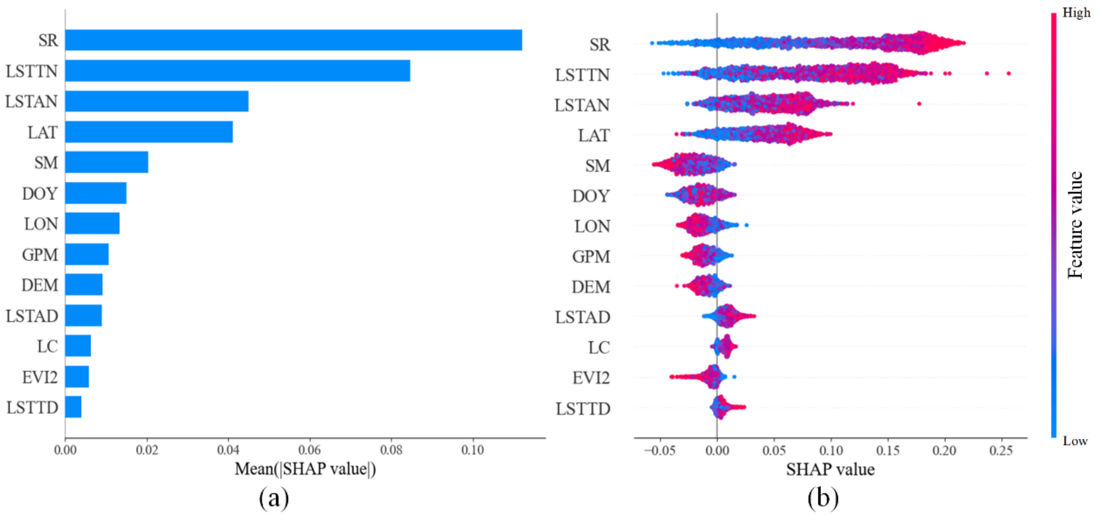

Fig. 11. Global feature importance analysis of the HyTC-TaNet model using SHAP. (a) Mean absolute SHAP values of all input features. (b) SHAP value distributions showing the direction and magnitude of each feature's impact on air temperature estimation.

5.2 Physical Interpretation of the Optimal Temporal Sequence

The identification of a 6–7 days optimal input sequence offers significant physical insights into the Ta estimation. Meteorologically, this duration corresponds to the characteristic lifecycle of synoptic weather systems in mid-latitudes (Holton and Hakim, 2013). Air temperature is not an instantaneous variable but a continuous trajectory governed by these multi-day weather patterns. A window of approximately one week enables the model to learn the contextual information of the current weather system, such as the accumulation of heat during a stagnant high-pressure system, thereby improving estimation robustness compared to shorter sequences.

Furthermore, the importance of this temporal sequence is reinforced by the thermodynamic properties of the study area, consistent with the feature importance rankings observed in Section 5.1. While SHAP analysis identifies SR as the primary driver, the LST time series is critical for modeling the phase shift in surface heating. Due to the thermal inertia of the underlying surface, particularly in regions with moist soil and vegetation, there is a physical time lag between SR and the response of Ta (Bechtel, 2015). The 6-7 days window allows the network to account for this cumulative heating effect, integrating the history of energy input required to heat the land-atmosphere system to its current state.

Finally, extending the input sequence beyond this threshold leads to performance saturation. This observation is consistent with the statistical concept of atmospheric memory, where the temporal correlation of Ta anomalies decays over time(Wilks, 2011). Data extending beyond the typical decorrelation time scale (approximately one week) lose their physical connection to the current state, acting as uncorrelated noise that complicates model optimization without providing valid predictive signals.

5.3 Spatial Generalization and Applicability Domain Analysis

To quantify the spatial transferability of the proposed model beyond standard station-based validation, we employed the AOA method. As shown in Fig. 12, the spatial reliability of the model is not uniform but is physically constrained by the representativeness of training data in the multidimensional feature space.

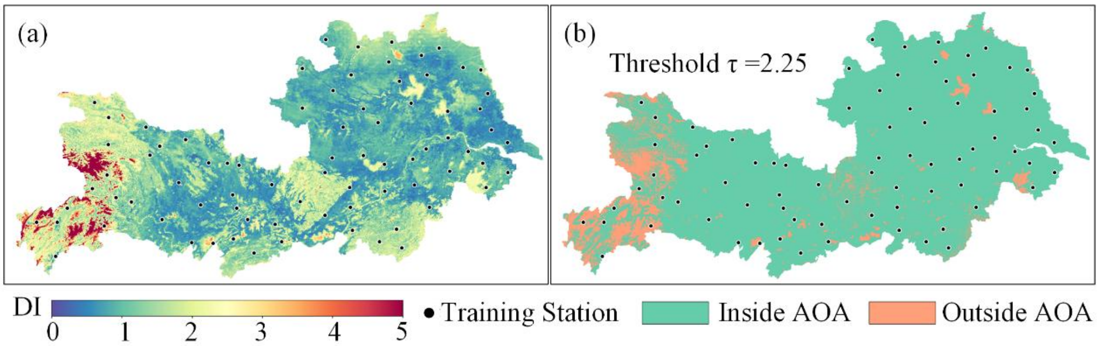

Fig. 12. Spatial assessment of model applicability. (a) The spatial distribution of the DI, overlaid with meteorological training stations (black dots). (b) The binary AOA map derived from the DI using a threshold of $\tau = 2.25$.

The DI map (Fig. 12(a)) reveals a clear "east-west reliability gradient" that aligns consistently with the density of meteorological stations. In the station-dense plains of Jiangsu and northern Anhui, widespread low DI values (blue) indicate that the environmental features are well-covered by the training samples, suggesting high statistical reliability. Conversely, high DI values (yellow to red) are clustered in the mountainous regions of western Hubei. This physically confirms that prediction uncertainty significantly increases in complex terrains lacking representative ground truth, highlighting the dependency of data-driven models on the training distribution.

The binary AOA map (Fig. 12(b)), derived using an adaptive threshold, further delineates the boundaries of reliability. Although the majority of the study area falls within the reliable domain ("Inside AOA"), distinct extrapolation clusters ("Outside AOA") are identified over large water bodies (e.g., Lake Taihu, Lake Hongze) and high-altitude ridges. This phenomenon is closely linked to the feature importance analysis (Fig. 11). SR was identified as the dominant predictor, followed by LST. Since the training stations are exclusively terrestrial, the distinct radiative and thermal properties of water surfaces create a significant deviation in the weighted feature space compared to land. Consequently, the AOA algorithm effectively flags these water bodies as extrapolation zones due to their unique environmental signatures. And it is important to note that being classified as "Outside AOA" does not necessarily imply erroneous predictions, but rather indicates a lack of direct statistical support from the training data.

6. Conclusion and future work

Although existing air temperature estimation approaches have achieved progress in capturing nonlinear relationships between multi-source variables and air temperature, their ability to model complex temporal interactions and to leverage historical sequences remains limited, and they lack explicit consideration of spatial uncertainty, underscoring the need for more advanced architectures and spatial assessments. To address these limitations, this study integrates multi-source time series data and introduces a hybrid model (HyTC-TaNet) that combines Transformer-based global dependency learning with CNN-based local feature extraction for high-precision temporal modeling, while simultaneously employing the AOA metric to explicitly quantify spatial uncertainty. Comprehensive comparisons among eight models, including the proposed HyTC-TaNet and seven benchmark algorithms, revealed that a temporal input length of 6-7 days yielded the best estimation performance across all models. Mechanistically, the SHAP-based interpretability analysis confirmed that the model successfully captures the thermodynamic phase shift and memory effects inherent in land-atmosphere interactions, providing a robust physical explanation for the identified optimal time window.

Among all tested models, HyTC-TaNet performs the best, achieving an RMSE of 1.429°C, MAE of 1.101°C, and R^2 of 0.976. Furthermore, beyond standard accuracy metrics, the AOA analysis rigorously defined the reliable monitoring boundaries of the model. This assessment highlighted the operational risks in data-sparse or topographically complex regions, ensuring that the generated high-resolution Ta maps are used with appropriate confidence. These findings highlight the critical role of temporal sequence optimization in enhancing model robustness and generalization for air temperature estimation tasks.

Despite the positive progress, there are still certain limitations. First, more effective LST data reconstruction and quality assurance of data availability need further exploration. Second, this study focuses solely on modeling and estimating daily air temperature, without addressing the ability to predict continuous multi-day air temperature variation trends, which limits the model's broader application. Future work should therefore focus on developing multi-day predictive frameworks that can jointly estimate and forecast air temperature dynamics, as well as exploring the deployment of such models in real-time monitoring and agricultural management systems. Furthermore, integrating additional meteorological and biophysical variables, along with advanced multi-source fusion strategies, may further enhance model interpretability and operational applicability.

CRediT authorship contribution statement

Li Liu: Writing – review & editing, Writing – original draft, Visualization, Validation, Software, Methodology, Formal analysis, Data curation, Supervision, Funding acquisition, Conceptualization. **Cian Yuan:** Writing – review & editing, Writing – original draft, Visualization, Validation, Software, Methodology, Formal analysis, Data curation, Supervision. **Jingfeng Huang:** Writing – review & editing, Methodology, Conceptualization, Supervision. **Yi Yu:** Writing – review & editing, Supervision. **Pan Shao:** Writing – review & editing, Supervision. **Junbo Yu:** Writing – review & editing, Supervision, Funding acquisition. **Lu Wang:** Writing – review & editing, Supervision. **Ran Huang:** Writing – review & editing, Visualization, Validation, Methodology, Supervision, Funding acquisition, Conceptualization. **Dong Ren:** Writing – review & editing, Supervision. **Thomas F. A. Bishop:** Writing – review & editing, Supervision. All the authors read and approved the final manuscript.

Declaration of competing interest

The authors declare that they have no known competing financial interests or personal relationships that could have appeared to influence the work reported in this paper.

Code availability

All codes are available at https://github.com/.......

Acknowledgments

The authors acknowledge the resources and supports provided by the Advanced Computing Center at the China Three Gorges University.

Funding

This work was supported by the National Natural Science Foundation of China (Grant Nos. 42101364, 42401404). It was also funded by the Natural Science Foundation of Hubei Province (Grant No. 2024AFB130), the National Key Research and Development Program of China (Grant No. 2024YFD1702005), the Platform Program funded by the Department of Science and Technology of Hubei Province (Grant No. 2024BSB002) and the Hubei Provincial Department of

Education Science and Technology Research Project (Grant No. Q20241202).

Data availability statement

The data that support the findings of this study are openly available in Zenodo at https://doi.org/.....(Liu et al., 2025b).

References:

Abhishek, A. et al., 2023. Dryspells and Minimum Air Temperatures Influence Rice Yields and their Forecast Uncertainties in Rainfed Systems. Agric. For. Meteorol. 341, 109683. http://doi.org/10.1016/j.agrformet.2023.109683

Bay, Y.Y. and Yearick, K.A., 2024. Machine learning vs deep learning: the generalization problem. arXiv preprint arXiv:2403.01621

Bechtel, B., 2015. A New Global Climatology of Annual Land Surface Temperature. Remote Sens. 7(3), 2850-2870. http://doi.org/10.3390/rs70302850

Benali, A. et al., 2012. Estimating air surface temperature in Portugal using MODIS LST data. Remote Sens. Environ. 124, 108-121. http://doi.org/10.1016/j.rse.2012.04.024

BREIMAN, L., 2001. 2001_random_forest. Mach. Learn.

Carrión, D. et al., 2021. A 1-km hourly air-temperature model for 13 northeastern U.S. states using remotely sensed and ground-based measurements. Environ. Res. 200, 111477. http://doi.org/10.1016/j.envres.2021.111477

Chen, T. and Guestrin, C., 2016. XGBoost: A Scalable Tree Boosting System. ACM

Chen, Y. et al., 2021. An all-sky 1 km daily land surface air temperature product over mainland China for 2003–2019 from MODIS and ancillary data. Earth Syst. Sci. Data. 13(8), 4241-4261. http://doi.org/10.5194/essd-13-4241-2021

Chung, U. et al., 2006. Minimum temperature mapping over complex terrain by estimating cold air accumulation potential. Agric. For. Meteorol. 137(1-2), 15-24. http://doi.org/10.1016/j.agrformet.2005.12.011

Dou, Y. et al., 2020. Mapping high temperature damaged area of paddy rice along the Yangtze River using Moderate Resolution Imaging Spectroradiometer data. Int. J. Remote Sens. 41(2), 471-486. http://doi.org/10.1080/01431161.2019.1643936

Elman, J.L., 1990. Finding Structure in Time. Cogn. Sci. 14(2), 179-211. http://doi.org/10.1207/s15516709cog1402_1

Gao, M. et al., 2021. Use of Google Earth Engine to Generate a 20-Year 1 Km × 1 Km Monthly Air Temperature Product Over Yellow River Basin. IEEE J. Sel. Top. Appl. Earth Observ. Remote Sens. 14, 10079-10090. http://doi.org/10.1109/JSTARS.2021.3116258

Good, E.J., 2016. An in situ-based analysis of the relationship between land surface “skin” and screen-level air temperatures. J. Geophys. Res.-Atmos. 121(15), 8801-8819. http://doi.org/10.1002/2016JD025318

Good, E.J. et al., 2017. A spatiotemporal analysis of the relationship between near-surface air temperature and satellite land surface temperatures using 17 years of data from the ATSR series. J. Geophys. Res.-Atmos. 122(17), 9185-9210. http://doi.org/10.1002/2017JD026880

Hartmann, D.L., 2016. Natural Climate ChangeGlobal Physical Climatology. Elsevier, pp. 361-395.

He, J. et al., 2020. The first high-resolution meteorological forcing dataset for land process studies over China. Sci. Data. 7(1), 25. http://doi.org/10.1038/s41597-020-0369-y

Hochreiter, S. and Schmidhuber, J., 1997. Long Short-Term Memory. Neural Comput. 9(8), 1735-1780. http://doi.org/10.1162/neco.1997.9.8.1735

Holton, J.R. and Hakim, G.J., 2013. IntroductionAn Introduction to Dynamic Meteorology. Elsevier, pp. 1-29.

Hooker, J. et al., 2018. A global dataset of air temperature derived from satellite remote sensing and weather stations. Sci. Data. 5(1), 180246. http://doi.org/10.1038/sdata.2018.246

Hou, P. et al., 2013. Near-surface air temperature retrieval from satellite images and influence by wetlands in urban region. Theor. Appl. Climatol. 111(1-2), 109-118. http://doi.org/10.1007/s00704-012-0629-7

Huang, R. et al., 2025a. A novel framework for dynamic and quantitative mapping of damage severity due to compound Drought–Heatwave impacts on tea Plantations, integrating Sentinel-2 and UAV images. Comput. Electron. Agric. 228, 109688. http://doi.org/10.1016/j.compag.2024.109688

Huang, R. et al., 2025b. A novel scheme for seamless global mapping of daily mean air temperature (SGM_DMAT) at 1-km spatial resolution using satellite and auxiliary data. Ecol. Inform. 90, 103266. http://doi.org/10.1016/j.ecoinf.2025.103266

Ji, F. et al., 2014. Evolution of land surface air temperature trend. Nat. Clim. Chang. 4(6), 462-466. http://doi.org/10.1038/nclimate2223

Lezama Valdes, L. et al., 2021. A Machine Learning Based Downscaling Approach to Produce High Spatio-Temporal Resolution Land Surface Temperature of the Antarctic Dry Valleys from MODIS Data. Remote Sens. 13(22), 4673. http://doi.org/10.3390/rs13224673

Li, W. et al., 2021. A Practical Remote Sensing Monitoring Framework for Late Frost Damage in Wine Grapes Using Multi-Source Satellite Data. Remote Sens. 13(16), 3231. http://doi.org/10.3390/rs13163231

Lin, S. et al., 2012. Evaluation of estimating daily maximum and minimum air temperature with MODIS data in east Africa. Int. J. Appl. Earth Obs. Geoinf. 18, 128-140. http://doi.org/10.1016/j.jag.2012.01.004

Liu, J. et al., 2022. An Analysis of Spatio-Temporal Relationship between Satellite-Based Land Surface Temperature and Station-Based Near-Surface Air Temperature over Brazil. Remote Sens. 14(17), 4420. http://doi.org/10.3390/rs14174420

Liu, L. et al., 2020. Optimal MODIS data processing for accurate multi-year paddy rice area mapping in China. GISci. Remote Sens. 57(5), 687-703. http://doi.org/10.1080/15481603.2020.1773012

Liu, L. et al., 2025a. SMN-AgroCLA: a deep learning framework with sequential midrange normalization for enhanced rice yield prediction using remote sensing data. GISci. Remote Sens. 62(1), 2569964. http://doi.org/10.1080/15481603.2025.2569964

Liu, L. et al., 2025b. Dataset for HyTC-TaNet: A Hybrid Deep Learning Model Capturing Multi-day Temporal Dependencies for Daily Mean Air Temperature Estimation with Spatial Applicability Analysis. Zenodo.

Lu, J. et al., 2025. Estimation of rice yield using multi-source remote sensing data combined with crop growth model and deep learning algorithm. Agric. For. Meteorol. 370, 110600. http://doi.org/10.1016/j.agrformet.2025.110600

Lundberg, S.M. and Lee, S., 2017. A unified approach to interpreting model predictions, Proceedings of the 31st International Conference on Neural Information Processing Systems. Curran Associates Inc.,

Long Beach, California, USA, pp. 4768–4777.
Ma, Y. et al., 2022. Agricultural Vulnerability Assessment of High-Temperature Disaster in Shaanxi Province of China. Agriculture-Basel. 12(7), 980. http://doi.org/10.3390/agriculture12070980
Marzban, F. et al., 2018. The influence of land-cover type on the relationship between NDVI–LST and LST-T_{air}. Int. J. Remote Sens. 39(5), 1377-1398. http://doi.org/10.1080/01431161.2017.1402386
Meyer, H. and Pebesma, E., 2021. Predicting into unknown space? Estimating the area of applicability of spatial prediction models. Methods Ecol. Evol. 12(9), 1620-1633. http://doi.org/10.1111/2041-210X.13650
Nieto, H. et al., 2011. Air temperature estimation with MSG-SEVIRI data: Calibration and validation of the TVX algorithm for the Iberian Peninsula. Remote Sens. Environ. 115(1), 107-116. http://doi.org/10.1016/j.rse.2010.08.010
Overland, J.E. et al., 2019. Surface air temperature. Arctic report card. 5
Pape, R. and Löffler, J., 2004. Modelling spatio-temporal near-surface temperature variation in high mountain landscapes. Ecol. Model. 178(3-4), 483-501. http://doi.org/10.1016/j.ecolmodel.2004.02.019
Prihodko, L. and Goward, S.N., 1997. Estimation of air temperature from remotely sensed surface observations. Remote Sens. Environ. 60(3), 335-346. http://doi.org/10.1016/S0034-4257(96)00216-7
Roberts, D.R. et al., 2017. Cross-validation strategies for data with temporal, spatial, hierarchical, or phylogenetic structure. Ecography. 40, 913-929
Robeson, S.M., 2002. Relationships between mean and standard deviation of air temperature: implications for global warming. Clim. Res. 22, 205-213. http://doi.org/10.3354/cr022205
Shanmugapriya, P. et al., 2019. Applications of Remote Sensing in Agriculture - A Review. International Journal of Current Microbiology and Applied Sciences. 8(01), 2270-2283. http://doi.org/10.20546/ijcmas.2019.801.238
Shin, J. et al., 2020. Seasonal forecasting of daily mean air temperatures using a coupled global climate model and machine learning algorithm for field-scale agricultural management. Agric. For. Meteorol. 281, 107858. http://doi.org/10.1016/j.agrformet.2019.107858
Song, P. et al., 2022. A 1 km daily surface soil moisture dataset of enhanced coverage under all-weather conditions over China in 2003–2019. Earth Syst. Sci. Data. 14(6), 2613-2637. http://doi.org/10.5194/essd-14-2613-2022
Sun, Y.J. et al., 2005. Air temperature retrieval from remote sensing data based on thermodynamics. Theor. Appl. Climatol. 80(1), 37-48. http://doi.org/10.1007/s00704-004-0079-y
Tang, W. et al., 2024. TRIMS LST: a daily 1 km all-weather land surface temperature dataset for China's landmass and surrounding areas (2000–2022). Earth Syst. Sci. Data. 16(1), 387-419. http://doi.org/10.5194/essd-16-387-2024
Ueyama, H., 2024. Compiling an hourly gridded dataset for surface air temperature at 50-m resolution using radiative cooling scale and numerical weather prediction model outputs. Agric. For. Meteorol. 350, 109991. http://doi.org/10.1016/j.agrformet.2024.109991
Vaswani, A. et al., 2017. Attention is all you need. Advances in neural information processing systems. 30
Wang, M. et al., 2024. Reconstruction of all-sky daily air temperature datasets with high accuracy in China from 2003 to 2022. Sci. Data. 11(1), 1133. http://doi.org/10.1038/s41597-024-03980-z
Wei, X. et al., 2024. The response of agricultural drought to meteorological drought modulated by air temperature. J. Hydrol. 639, 131626. http://doi.org/10.1016/j.jhydrol.2024.131626
Wilks, D.S., 2011. Forecast VerificationInternational Geophysics. Elsevier, pp. 301-394.

Wu, T. and Li, Y., 2013. Spatial interpolation of temperature in the United States using residual kriging. Appl. Geogr. 44, 112-120. http://doi.org/10.1016/j.apgeog.2013.07.012

Xu, C. et al., 2023. Air temperature estimation over winter wheat fields by integrating machine learning and remote sensing techniques. Int. J. Appl. Earth Obs. Geoinf. 122, 103416. http://doi.org/10.1016/j.jag.2023.103416

Xu, Q. et al., 2025. A multimodal machine learning fused global 0.1° daily evapotranspiration dataset from 1950-2022. Agric. For. Meteorol. 372, 110645. http://doi.org/10.1016/j.agrformet.2025.110645

Xu, S. and Cheng, J., 2021. A new land surface temperature fusion strategy based on cumulative distribution function matching and multiresolution Kalman filtering. Remote Sens. Environ. 254, 112256. http://doi.org/10.1016/j.rse.2020.112256

Yang, K. et al., 2010. On downward shortwave and longwave radiations over high altitude regions: Observation and modeling in the Tibetan Plateau. Agric. For. Meteorol. 150(1), 38-46. http://doi.org/10.1016/j.agrformet.2009.08.004

Yang, S. et al., 2024. Deep Learning for Near-Surface Air Temperature Estimation From FengYun 4A Satellite Data. IEEE J. Sel. Top. Appl. Earth Observ. Remote Sens. 17, 13108-13119. http://doi.org/10.1109/JSTARS.2023.3322343

Yu, Y. et al., 2024. Solar zenith angle-based calibration of Himawari-8 land surface temperature for correcting diurnal retrieval error characteristics. Remote Sens. Environ. 308, 114176. http://doi.org/10.1016/j.rse.2024.114176

Yu, Y. et al., 2025. Spatial Soil Moisture Prediction From In Situ Data Upscaled to Landsat Footprint: Assessing Area of Applicability of Machine Learning Models. IEEE Trans. Geosci. Remote Sensing. 63, 1-19. http://doi.org/10.1109/TGRS.2025.3565818

Zhang, H. et al., 2016. Estimating daily air temperatures over the Tibetan Plateau by dynamically integrating MODIS LST data. J. Geophys. Res.-Atmos. 121(19). http://doi.org/10.1002/2016JD025154

Zhang, L. et al., 2014. A review on air temperature estimation by satellite thermal infrared remote sensing. Journal of Natural Resources. 29(3), 540-552

Zhang, R. et al., 2015. A Remote Sensing Method for Estimating Surface Air Temperature and Surface Vapor Pressure on a Regional Scale. Remote Sens. 7(5), 6005-6025. http://doi.org/10.3390/rs70506005

Zhang, T. et al., 2022. A global seamless 1 km resolution daily land surface temperature dataset (2003–2020). Earth Syst. Sci. Data. 14(2), 651-664. http://doi.org/10.5194/essd-14-651-2022

Zhang, X. et al., 2021. A practical reanalysis data and thermal infrared remote sensing data merging (RTM) method for reconstruction of a 1-km all-weather land surface temperature. Remote Sens. Environ. 260, 112437. http://doi.org/10.1016/j.rse.2021.112437

Zhao, K. et al., 2025. A 1-km daily high-accuracy meteorological dataset of air temperature, atmospheric pressure, relative humidity, and sunshine duration across China (1961–2021). Earth System Science Data Discussions. 2025, 1-30. http://doi.org/10.5194/essd-2025-291

Zhu, W. et al., 2013. Estimation of daily maximum and minimum air temperature using MODIS land surface temperature products. Remote Sens. Environ. 130, 62-73. http://doi.org/10.1016/j.rse.2012.10.034

Žížala, D. et al., 2022. High-resolution agriculture soil property maps from digital soil mapping methods, Czech Republic. Catena. 212, 106024. http://doi.org/10.1016/j.catena.2022.106024